d·Collection

이학석사 학위논문

Optoelectronic Characteristics Prediction and Optimization of Flash-Evaporated Perovskite Photodetectors

플래시증착 페로브스카이트 기반 광검출기의 광전자
특성 예측 및 최적화 연구

2021 년 8 월

서울대학교 대학원
물리·천문학부
이 종 훈

Optoelectronic Characteristics Prediction and Optimization of Flash-Evaporated Perovskite Photodetectors

지도 교수 이 탁 희

이 논문을 이학석사 학위논문으로 제출함

2021 년 7 월

서울대학교 대학원

물리·천문학부 물리학 전공

이 종 훈

이종훈의 이학석사 학위논문을 인준함

2021 년 7 월

위 원 장		최 석 봉
부위원장		이 탁 희
위 원		차 국 린

Abstract

Optoelectronic Characteristics Prediction and Optimization of Flash-Evaporated Perovskite Photodetectors

Jonghoon Lee

Department of Physics and Astronomy

Seoul National University

Organic-inorganic halide perovskites (OHPs) have recently received enormous attention due to their excellent properties for optoelectronic and electronic devices. Out of various deposition methods studied in the field, solution-processing, chemical vapor deposition (CVD) and thermal evaporation have gained the most attention for OHPs. Spin-coating techniques of OHPs are mainly used in lab-scale device fabrication because it is a low-cost and easily accessible process. Although some works have reported remarkable device performances in large-area perovskite optoelectronic devices made with spin-coated perovskite films, the spin-coating techniques face a challenge in producing reliable and uniform films over a large area.

To overcome this, single-source flash evaporation technique, in which a single source of materials of interest is rapidly heated to be deposited in a few seconds, is one of the candidate techniques for large-scale thin film deposition of OHPs. In my first study, I investigated the reliability and controllability of the single-source flash evaporation technique for methylammonium lead iodide (MAPbI$_3$) perovskite. In-depth statistical analysis was employed to demonstrate that the MAPbI$_3$ films prepared via the flash evaporation have an ultrasmooth surface and uniform thickness throughout the 4-inch

wafer scale. I also show that the thickness and grain size of the MAPbI$_3$ film can be controlled by adjusting the amount of the source and number of deposition steps. In addition, I demonstrate that the reliability of the technique has a direct impact on the device characteristics of the fabricated photodetector devices via statistical analysis.

However, due to a complex nature of the different experimental parameters involved in the deposition process, it is not straightforward to obtain the optimal condition for producing high-quality OHP films. In my second study, I tackled this problem by employing the design-of-experiment (DOE) process, which is an efficient statistical analysis for finding an optimized condition with a minimized number of experiments. The DOE process was used for optimizing the responsivity of the OHP photodetector devices against the input variables used in the deposition that yielded an enhanced responsivity of 112.2 mA/W, which is up to an order of magnitude higher than that of the unoptimized devices. The experimental results using the DOE method provide not only the conditions required for enhancing the device performance but also the guidelines for improving the overall film quality through exploring the variable space of the flash evaporation technique.

Keywords: Flash-evaporation, Perovskite, Photodetector, Modeling, Design-of-Experiment

Student Number: 2019-24566

List of Contents

iv

List of Figures

Chapter 2.

Figure 2.1. (a) Schematic illustration of $MAPbI_3$ crystal structure. (b) Schematic illustration of deposition of organo-halide perovskite film via flash evaporation. The inset shows photographs of $MAPbI_3$ single crystal powder. (c) A photograph of the substrate holder for film uniformity test with the labels that indicate the location of the substrates (from A to F). Adapted from Lee et al.

Figure 2.2. (a) An optical microscope image of the flash evaporated $MAPbI_3$ film. (b) SEM image and (c) AFM images of flash evaporated $MAPbI_3$ film surface. Adapted from Lee et al.

Figure 2.3. (a) XRD data of the flash evaporated film, spin-coated film and single crystal powder. Calculated results from the unit cell of $MAPbI_3$ are also shown. (b) UV-visible absorbance and PL spectra of $MAPbI_3$ film deposited via flash evaporation. The inset shows Tauc plot to estimate the optical bandgap of the perovskite film. Adapted from Lee et al.

Figure 2.4. Uniformity test of flash evaporated $MAPbI_3$ films. (a) Cross-sectional SEM images for the thickness comparison of the $MAPbI_3$ film by the substrate location given in Fig. 1(c). (b) The measured thickness values presented in box and whisker diagram at each location.　(c) A histogram of all the thickness data. (d) Comparison circles from the Tukey test. (e) Color map image of the average thickness values at each substrate location on the 4-inch wafer. (f) The estimated thickness of the perovskite film by Gaussian process. (g) UV-visible absorbance spectra of the $MAPbI_3$ films at the different substrate locations. Adapted from Lee et al.

Figure 2.5. (a) A graph of thickness of the flash evaporated perovskite film as a function of the amount of the MAPbI$_3$ single crystal power source. (b) Cross-sectional SEM images for a single- and multi-step deposited perovskite films by flash evaporation for comparison. (c) Top-view SEM images for showing grain size variation for deposition with different source mass. (d) Grain size correlation graph of the deposited perovskite films according to the source mass. The inset shows a predicted controllable range of the grain size and thickness of the MAPbI$_3$ films by the empirical fit shown as the dashed line. Adapted from Lee et al.

Figure 2.6. Device characteristics of photodetectors prepared by flash evaporation. (a) I-V characteristics under 520 nm laser with different intensities. The inset shows the optical microscope image of the fabricated MAPbI$_3$ photodetector. (b) Time-dependent photoresponse of the photodetector under few cycles of turn-on and off. (c) The I-V characteristics under light and dark conditions for the photodetectors prepared by the flash evaporated films at the different substrate locations. Adapted from Lee et al.

Chapter 3.

Figure 3.1. (a) A graphical representation of the Box-Behnken design for three factors (heating current, source mass, and excess MAI ratio). (b) A schematic illustration of single-source flash evaporation to deposit a MAPbI$_3$ film. (c) surface and (d) cross-sectional SEM images, and (e) an AFM image of the flash-evaporated MAPbI$_3$ film. (f) X-ray diffraction pattern of the flash-evaporated MAPbI$_3$ film (red) and calculated data (black) from the unit cell of MAPbI$_3$. (g) UV-visible absorbance spectra (blue) and PL spectra (red) of the MAPbI$_3$ film (h) I-V characteristics of flash-evaporated perovskite photodetectors under white light illumination (red) and dark (black) conditions, which were used to extract responsivity (R) and specific detectivity (D*). Adapted from Lee et al.

Figure 3.2. (a) Multi-variable correlation matrix plot. (b) Representative correlation graphs for source mass and film thickness, grain size and PL peak position, relative purity and off current, and responsivity and surface roughness. The ellipses in the graphs show the regions with the confidence level of 90 %. Adapted from Lee et al.

Figure 3.3. (a) A 3D scattering plot of the film thickness according to the heating current, source mass, and excess MAI ratio (MAI/MAPbI$_3$) from the regression analysis. (b) A contour plot of the film thickness according to the heating current and the source mass. (c) Graphs of the film thickness as a function of the source mass at the different heating currents of 60 A (green line), 100 A (orange line), and 140 A (black line). (d), (e), and (f) are the same graphs as (a), (b) and (c) but represent the grain size instead of the film thickness. Adapted from Lee et al.

Figure 3.4. 3D scattering plots of (a) the responsivity and (c) the relative purity according to the heating current, source mass, and MAI/MAPbI$_3$ from the regression analysis. Contour plots of (b) responsivity and (d) the relative purity are extracted from 3D scattering data (Fig. 4a and c) at the source mass of 300, 500, 700 mg. Adapted from Lee et al.

Figure 3.5. (a) I-V characteristics of white light illuminated photodetectors with three different MAPbI$_3$ films which are flash-evaporated under the optimized (red), central (black), and worst (blue) deposition condition. The inset shows log-scale I-V curves of the optimized photodetector under white light illumination (red) and dark (black) conditions. (b) The predicted responsivity values from the regression model (white) and experimental values (red) under various deposition conditions. Device characteristics of the photodetectors prepared by the optimized deposition conditions. (c) I-V characteristics under 520 nm laser illumination with different intensities. (d) Photoresponsivity and detectivity of the flash evaporated

MAPbI$_3$ photodetectors operated at a bias voltage of 20 V as a function of the incident laser power, both of which decrease with power, as expected. Adapted from Lee et al.

Chapter 1. Introduction

1.1. Brief introduction of perovskite

Perovskites have a crystalline structure witch chemical formaula ABX_3, where A is organic or inorganic cation (e.g, methylammonium, formamidium), B is a divalent metal (e.g, Pb, Sn), and X is a halide anion (e.g, Cl, Br, I).[1-2] In the 3D ABX_3 cubic crystal structure, B cation is located in the middle of the six halide anions and A is located at the vertex of the hexahedron.

The mechanism of bandgap formation in metal halide perovskite crystals is still debated, emission wavelength of perovskite can be easily tuned by totally or partially replacing B cations and X anions. Perovskites materials are characterized by high color purity, wide bandgap tunability, high charge carrier mobility, and low material cost. Therefore, they have great advantages in mass production and commercialization.[3] Because of their excellent properties for optoelectronic and electronic devices, organic-inorganic halide perovskites   have recently received enormous attention.

1.2. Perovskite fabrication method for electrical device

In order to make and use the perovskite material as a device, it is necessary to proceed with the process of fabricating a film. Out of various deposition methods studied in the field, solution-processing[4-5], chemical vapor deposition (CVD)[6-7] and thermal evaporation[8-9] have gained the most attention for OHPs. Spin-coating techniques of metal halide perovskites are mainly used in lab-scale device fabrication because it is a low-cost and easily accessible process. Although some works have reported remarkable device performances in large-area perovskite optoelectronic devices made with spin-coated

perovskite films,[10, 11] the spin-coating techniques an cause damage to the lower layer and face a challenge in producing reliable and uniform films over a large area.

1.3.   Flash-evaporation method for large-scale device fabrication

Evaporation methods, which include dual-source vacuum deposition, sequential-partial pressure, mixed solution and vapor deposition, modified chemical vapor deposition method and single-source deposition, have shown a potential for producing uniform films over a large area.[2, 12] The evaporation methods do not require the use of solvents and thus have the advantage that the films can be deposited without solvent-induced-damages which are critical for organo-metal-halide perovskite films.[13-14] Organo-halide precursor (e.g. methylammonium iodide, MAI) and lead-source precursor (e.g. lead iodide, PbI_2) can be thermally evaporated by various methods, i.e., co-evaporation method,[15-16] vapor-assisted deposition[17] or sequential deposition[18-20] to fabricate organic halide perovskite (e.g. methylammonium lead iodide, $MAPbI_3$) films.

1.4.   Optimization process by Design-of-experiment

The one-factor-at-a-time (OFAT) method, which is commonly used as a systematic experimental method, has clear disadvantages that it is relatively time-consuming and does not consider interaction effects because only one input variable is considered at a time. Moreover, most of the experimental designs typically require a long time to gather a sufficiently large training data set. Even after the model is completed, precise data predictions are limited to the variables within the range of the training data set.

On the contrary, the design-of-experiment (DOE) approach[21] is a multivariate

statistical method that is optimized for minimal experimentation. In addition, the DOE method allows us to consider the correlation between the variables in the analysis step and discover optimal experimental conditions via regression analysis. Because the DOE approach considers various variables simultaneously, it is an efficient tool for achieving experimental targets in a relatively short period of time, given that a clear objective is set. Although the DOE approach remains as a powerful tool for performing multivariate statistical analysis, it has been rarely used for investigating the film deposition conditions of organo-metal-halide perovskites.[22] In my study, the DOE approach was used to analyze the relationship between the variables that affect the film deposition in the flash evaporation method, which in turn, provided guidelines for optimizing the deposition conditions that produce high-quality perovskite films with the desired optoelectronic properties. Our developed flash evaporation method was recently shown to be highly reproducible and only had few control variables, both of which are suitable for employing the DOE approach for optimizing the film quality.

References

[1] Park, N.-G. 2018 MRS Bull. 43, 527-533.

[2] Ávila J, Momblona C, Boix P P, Sessolo M and Bolink H J 2017 Joule 1 431-42.

[3] Kim, Y.-H., Kim, J. S. & Lee, T.-W. Strategies to Improve Luminescence Efficiency of Metal-Halide Perovskites and Light-Emitting Diodes. 2019 Adv. Mater. 31, 1804595.

[4] Nie W, Tsai H, Asadpour R, Blancon J-C, Neukirch A J, Gupta G, Crochet J J, Chhowalla M, Tretiak S, Alam M A, Wang H-L and Mohite A D 2015 Science 347 522.

[5] Yu W, Li F, Yu L, Niazi M R, Zou Y, Corzo D, Basu A, Ma C, Dey S, Tietze M L, Buttner U, Wang X, Wang Z, Hedhili M N, Guo C, Wu T and Amassian A 2018 Nat. Commun. 9 5354.

[6] Niu L, Liu X, Cong C, Wu C, Wu D, Chang T R, Wang H, Zeng Q, Zhou J, Wang X, Fu W, Yu P, Fu Q, Najmaei S, Zhang Z, Yakobson B I, Tay B K, Zhou W, Jeng H T, Lin H, Sum T C, Jin C, He H, Yu T and Liu Z 2015 Adv. Mater. 27 7800-8.

[7] Lan C, Dong R, Zhou Z, Shu L, Li D, Yip S and Ho J C 2017 Adv. Mater. 29 1702759.

[8] Momblona C, Gil-Escrig L, Bandiello E, Hutter E M, Sessolo M, Lederer K, Blochwitz-Nimoth J and Bolink H J 2016 Energy Environ. Sci. 9 3456-63.

[9] Mitzi D B, Prikas M T and Chondroudis K 1999 Chem. Mater. 11 542-4.

[10] Zhao X and Tan Z-K 2020 Nat. Photonics 14 215-8.

[11] Chen Y, Zhang L, Zhang Y, Gao H and Yan H 2018 RSC Adv. 8 10489-508.

[12] Li G, Ho J Y L, Wong M and Kwok H-S 2016 physica status solidi (RRL) – Rapid Research Letters 10 153-7.

[13] Sessolo M, Momblona C, Gil-Escrig L and Bolink H J 2015 MRS Bull. 40 660-6.

[14] Crane M J, Kroupa D M, Roh J Y, Anderson R T, Smith M D and Gamelin D R 2019 ACS Applied Energy Materials 2 4560-5.

[15] Du P, Li J, Wang L, Liu J, Li S, Liu N, Li Y, Zhang M, Gao L, Ma Y and Tang J 2019 ACS Appl. Mater. Interfaces 11 47083-90.

[16] Liu M, Johnston M B and Snaith H J 2013 Nature 501 395-8.

[17] Ono L K, Wang S, Kato Y, Raga S R and Qi Y 2014 Energy Environ. Sci. 7 3989-93.

[18] Yang D, Yang Z, Qin W, Zhang Y, Liu S and Li C 2015 J. Mater. Chem. A 3 9401-5.

[19] Chen C-W, Kang H-W, Hsiao S-Y, Yang P-F, Chiang K-M and Lin H-W 2014 Adv. Mater. 26 6647-52.

[20] Hwang B and Lee J-S 2017 Adv. Mater. 29 1701048.

[21] Antony J 2014 *Design of experiments for engineers and scientists*: Elsevier.

[22] Tyagi P, David T W, Stoichkov V D and Kettle J 2019 *Sol. Energy* **193** 12-9.

Chapter 2. Controllable deposition of organic metal halide perovskite films with wafer-scale uniformity by single source flash evaporation

In this thesis, I described flash-evaporation of perovskite films. Conventional solution-processing techniques such as the spin-coating method have been used successfully to reveal excellent properties of organic-inorganic halide perovskites (OHPs) for optoelectronic devices such as solar cell and light-emitting diode, but it is essential to explore other deposition techniques compatible with large-scale production. Single-source flash evaporation technique, in which a single source of materials of interest is rapidly heated to be deposited in a few seconds, is one of the candidate techniques for large-scale thin film deposition of OHPs. In this work, I investigated the reliability and controllability of the single-source flash evaporation technique for methylammonium lead iodide (MAPbI$_3$) perovskite. In-depth statistical analysis was employed to demonstrate that the MAPbI$_3$ films prepared via the flash evaporation have an ultrasmooth surface and uniform thickness throughout the 4-inch wafer scale. I also show that the thickness and grain size of the MAPbI$_3$ film can be controlled by adjusting the amount of the source and number of deposition steps. Finally, the excellent large-area uniformity of the physical properties of the deposited thin films can be transferred to the uniformity in the device performance of MAPbI3 photodetectors prepared by flash evaporation which exhibited the responsivity of 51 mA/W and detectivity of 9.55×10^{10} Jones.

2.1. Introduction

Organo-metal halide perovskites (OHPs) have come into the spotlight as the power conversion efficiency of solar cell using OHPs has increased dramatically in the past few years[1-7]. Since then, OHPs have demonstrated compliant performance in other optoeletronic devices such as light emitting diodes (LEDs)[8-12], photodetectors[13, 14],

lasers[15] and phototransistors[16]. Out of various methods studied in the field, solution-processing[2, 17, 18], thermal evaporation[19, 20] and chemical vapor deposition[21, 22] have gained the most attention as methods for depositing OHP thin films. Especially, spin-coating is the most commonly used lab-scale deposition method because it is a low-cost and easily accessible process. Although some works have reported remarkable device performances in large-area perovskite optoelectronic devices made with spin-coated perovskite films[9, 23], the solution-process fundamentally imposes limitations in reliably producing uniform films over a large area. In addition, the spin-coating methods have evolved to achieve high-quality OHP films for state-of-the-art devices by adopting additional techniques[17] such as hot-casting[2, 5], solvent engineering[24, 25] and two-step sequential deposition[3, 26, 27], which inevitably adds complexities, and therefore reduces the overall controllability of the process.

The evaporation method, on the other hand, has a potential for uniform large-area film deposition[28, 29], conformal film deposition on uneven surfaces[30], as well as a simple patterning with shadow masks[31]. Additionally, since it is a solvent-free process, there is no need to consider surface tension or solubility of the underlying layer. Organo-halide precursor (e.g. methylammonium iodide, MAI) and lead-source precursor (e.g. lead iodide, PbI_2) can be thermally evaporated by co-evaporation method[19, 32], sequential deposition[33-35] or vapour-assisted deposition[36, 37] to form OHP (e.g. methylammonium lead iodide, $MAPbI_3$) films. Although these deposition methods are well-established, it is still challenging to produce OHP films with the desired stoichiometric ratio between the three different ionic components by evaporation because the precursors have very different vaporization temperatures[28].

Flash evaporation method has gained attention as a candidate for evaporating two

7

or more precursors from a single thermal source by rapidly raising the temperature in a very short time[20, 30, 31, 38-41]. In principle, the rapid vaporization of the precursors induces complete and uniform evaporation of the precursors, while maintaining the same ratio between the different components in OHP. Solar cells with flash evaporated OHP films have exhibited over 10% of power conversion efficiency[39, 41], which is comparable to the early stage spin-coated OHP films[17, 42]. Furthermore, the flash evaporation method has been expanded to deposit OHP films with mixed cation and halide species[30], which is challenging for the aforementioned other evaporation methods[28]. Although this aspect of flash evaporation presents a prospect of exploring a diverse compositional range of OHPs, there has been relatively a few reports which have systematically studied the controllability of the flash evaporation method and the uniformity of OHP films produced by this method. Especially, flash evaporated OHP films have only been reported to be uniform in small areas, but wafer-scale uniformity has rarely been investigated to assess its applicability for mass-producing devices with uniform performance. In this paper, I demonstrate that OHP films with wafer-scale uniformity can be formed by flash evaporation. In addition, it is difficult to monitor the deposition rate and control the resulting film thickness with flash evaporation due to the rapid nature of the evaporation process, unlike other methods. For optoelectronic devices, the thickness of the active layer is critical in determining the device performance[43, 44]. Therefore, a reliable deposition of OHP films with controllability over a wide range of target thicknesses is desired for meeting different requirements in terms of film characteristics for various device applications. Our study directly shows that the thickness of flash evaporated OHP films can be controlled by simply adjusting the mass of the source material. Similarly, I discovered that the grain size of the flash evaporated OHP films varied with the mass of the source

materials loaded, and that the grain size could even be controlled by introducing multi-step depositions.

2.2. Results and Discussion

In this study, I focused on the deposition of MAPbI$_3$ films (see Figure 2.1(a) for the crystal structure) by flash evaporation. Figure 2.1(b) shows a schematic image of the flash evaporation process adopted in this work. The pre-synthesized MAPbI$_3$ single crystal powder was used as the source instead of PbI$_2$ and MAI precursors (see the inset of Figure 2.1(b)) in order to obtain better quality films owing to an exact stoichiometric ratio between
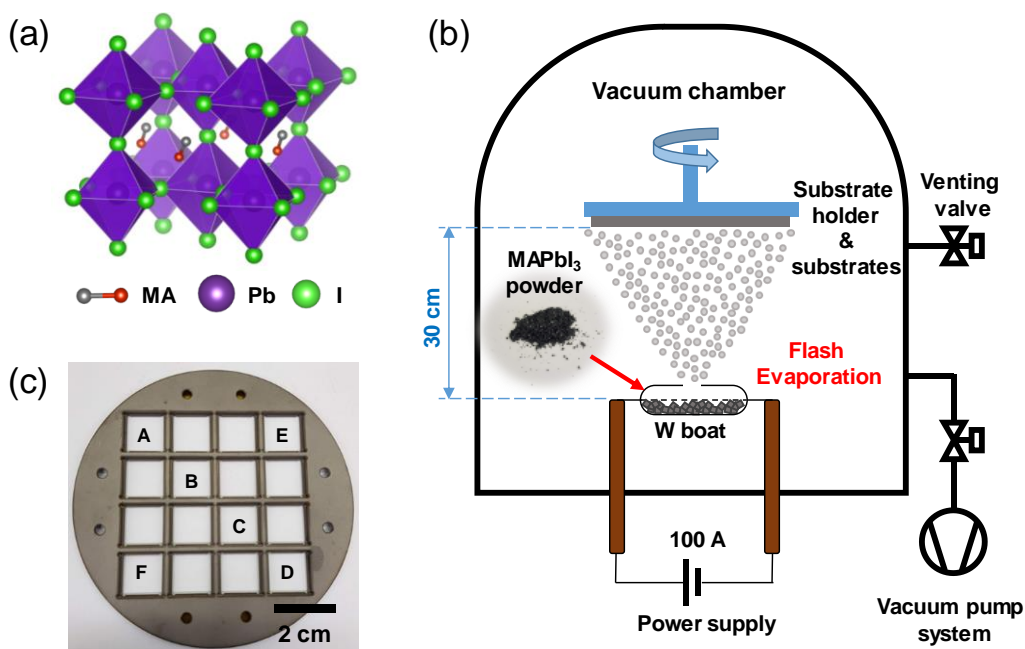
Figure 2.1 (a) Schematic illustration of MAPbI$_3$ crystal structure. (b) Schematic illustration of deposition of organo-halide perovskite film via flash evaporation. The inset shows photographs of MAPbI$_3$ single crystal powder. (c) A photograph of the substrate holder for film uniformity test with the labels that indicate the location of the substrates (from A to F).

the different ionic components of MAPbI$_3$ within the single crystal[30, 45]. The exact

amount of single crystal powder was loaded on the tungsten boat which is located inside of vacuum chamber. The source-to-substrate distance was designed to be 30 cm which is the longest distance among source-to-substrate distances of flash evaporation reported so far[20, 31, 38, 40, 41]. This is so that I could achieve a uniform deposition of MAPbI$_3$ over a large area at the substrate end. The MAPbI$_3$ single crystal powder was heated by rapidly ramping up the heater current to 100 A in 3 seconds at a constant voltage of 0.31 V. The powder was then evaporated within 60 seconds and deposited on substrates which were located on specific locations of the holder. Throughout this paper, I will refer to different sample locations in the 4-inch wafer size substrate holder as labeled in Figure 2.1(c) (substrate location A to F) to assess the uniformity of the deposited MAPbI$_3$ film.

I checked the film quality of flash evaporated MAPbI$_3$ films by probing their structural and optical properties as shown in Figures 2.2 and 2.3. An optical micrograph of the flash evaporated MAPbI$_3$ film patterned by a shadow mask showed a smooth and clean film with a clearly distinguishable boundary at the edge (see Figure 2.2(a)). The top-surface images of the films measured by field emission scanning electron microscope (FE-SEM) and atomic force microscope (AFM) are presented in Figures 2.2(b) and 2.2(c), respectively. A typical grain size determined from the FE-SEM image is 40 nm which I will discuss further later in the paper. A smooth and pinhole-free surface was observed with the roughness of approximately 5 nm (2.86 nm locally, Figure 2.2(c)).

Figure 2.3(a) shows the X-ray diffraction (XRD) results. The green line shows the XRD result of the single crystal powders of MAPbI$_3$ used as the source, which closely resembles the calculated XRD results. It signifies that a high purity MAPbI$_3$ single crystal powders were successfully synthesized. The blue and red lines show the XRD results of the flash evaporated and spin-coated MAPbI$_3$ films, respectively. The positions of the (110)

and (220) peaks were the same for all the XRD results (14.1º and 28.5º, respectively), confirming the identical crystal structure of the flash evaporated $MAPbI_3$ film with those prepared by other methods. As no peaks other than (110) and (220) peaks appeared, the deposited $MAPbI_3$ films exhibit a strong preferred orientation along the (110) surface[30, 32, 46, 47]. In addition, the high purity of the flash evaporated film is indicated by the absence of diffraction peaks that correspond to PbI_2 (asterisk marks (12.6º)). Note that this is an interesting observation because many previous studies [31, 38, 40, 41] have demonstrated that the addition of excess MAI was necessary to deposit pure $MAPbI_3$ films without PbI_2 impurities.

Figure 2.2 (a) An optical microscope image of the flash evaporated $MAPbI_3$ film.
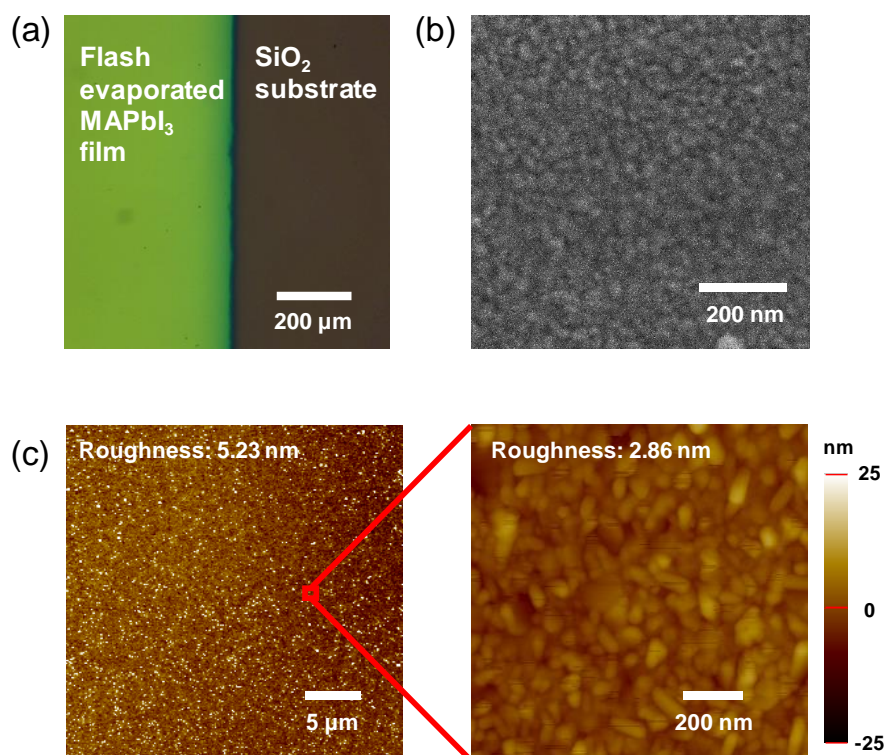
(b) SEM image and (c) AFM images of flash evaporated $MAPbI_3$ film surface.

UV-visible absorbance and photoluminescence (PL) spectra were taken to investigate the optical properties of the flash evaporated MAPbI$_3$ film (see Figure 2.3(b)). The estimated optical bandgap from the absorbance spectrum by using the Tauc plot[48] is 1.61 eV (see the inset of Figure 2.3(b)) and PL peak is shown at 756 nm with a full-width-half-maximum (FWHM) of 45 nm, both of which agree well with the reported values for MAPbI$_3$ in literature[15, 49]. When compared with the spin-coated MAPbI$_3$ film produced as a reference sample, it showed similar absorbance and PL spectra. From the structural and optical characterizations, I could safely confirm that our flash evaporated MAPbI$_3$ films had a high film quality without a significant amount of impurities formed.

I checked that the evaporated perovskite films had a uniform thickness and the same optical properties over the whole wafer. Before testing wafer-scale film uniformity, I compared the film uniformity between the flash evaporated perovskite film to spin-coated perovskite film (reference) on the 1.5 × 1.5 cm^2 substrate. The thickness values of both films were measured by randomly selecting 20 points on cross-sectional FE-SEM images.

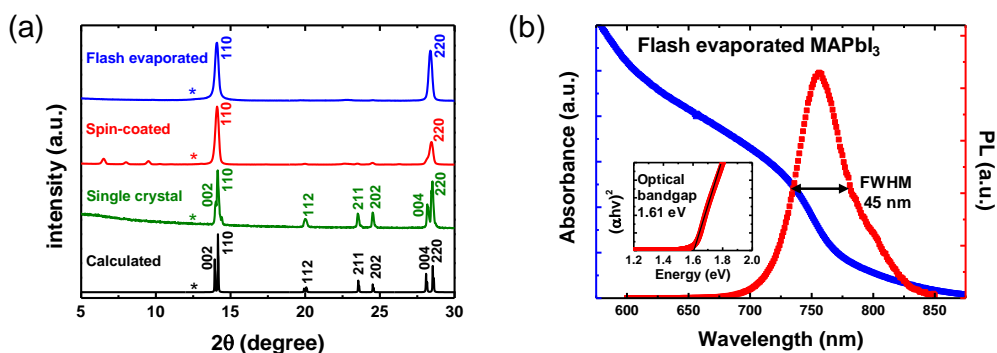**Figure 2.3** (a) XRD data of the flash evaporated film, spin-coated film and single crystal powder. Calculated results from the unit cell of MAPbI$_3$ are also shown. (b) UV-visible absorbance and PL spectra of MAPbI$_3$ film deposited via flash evaporation. The inset shows Tauc plot to estimate the optical bandgap of the perovskite film.

The average thickness values of the flash evaporated and spin-coated films were similar (207.1 nm and 225.0 nm, respectively), while the standard deviation for the spin-coated film was about 10 times larger (30.2 nm compared to 3.0 nm for the flash evaporated film). Given that the standard deviation value of 3.0 nm for the flash evaporated film is similar to the surface roughness value measured by AFM, the variation in the sampled thickness values can be assumed to be due to the morphology, not the variation in the actual thickness within the film. It can be seen that the film made by flash evaporation has a much uniform thickness and a smooth surface.

In order to investigate whether there was a change in the thickness depending on
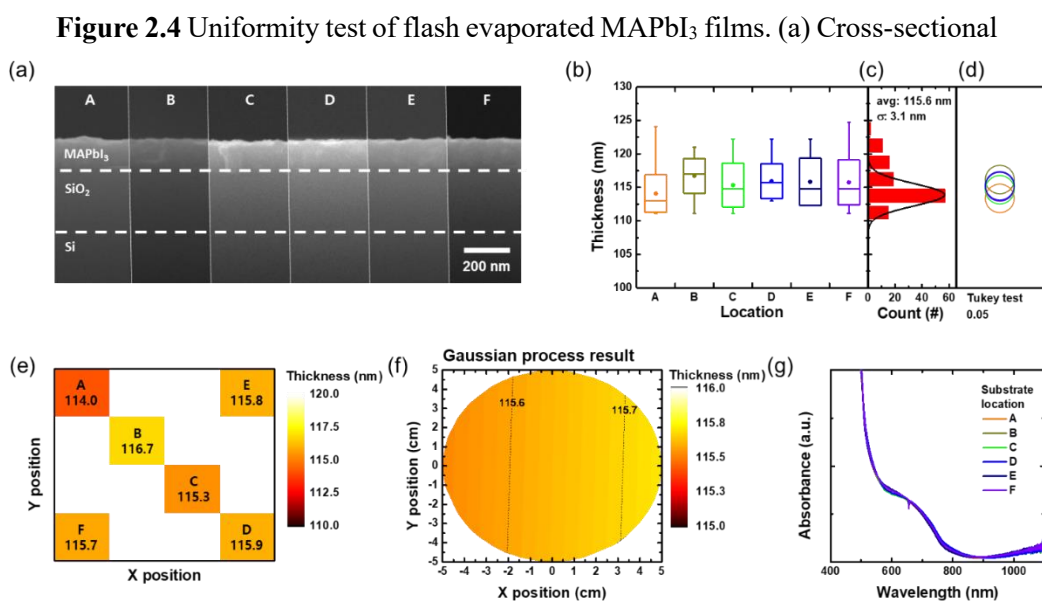
Figure 2.4 Uniformity test of flash evaporated MAPbI$_3$ films. (a) Cross-sectional

SEM images for the thickness comparison of the MAPbI$_3$ film by the substrate location given in Figure 1(c). (b) The measured thickness values presented in box and whisker diagram at each location. (c) A histogram of all the thickness data. (d) Comparison circles from the Tukey test. (e) Color map image of the average thickness values at each substrate location on the 4-inch wafer. (f) The estimated thickness of the perovskite film by Gaussian process. (g) UV-visible absorbance spectra of the MAPbI$_3$ films at the different substrate locations.

the location over the 4-inch wafer, cross-sectional FE-SEM images were taken for the evaporated films at each substrate location labeled according to Figure 2.1(c) (Figure 2.4(a)). The thickness values were measured at 20 points of the film for each substrate in order to carry out statistical analysis. Figure 2.4(b) is a graph summarizing the thickness values extracted from each substrate location drawn as a box and whisker diagram. The dots within the boxes represent the average values and boxes show the first and third quartile range of each distribution. The lines inside the box represent median values and the whiskers show the minimum and maximum values. The box and whisker diagrams show the similarity in the distribution of the thickness values at different locations. Figure 2.4(c) shows the distribution for all the measured 120 thickness values from the different locations shown in Figure 2.4(b) plotted together in one histogram. The thickness values did not significantly deviate from the average value of 115.6 nm (the standard deviation was 3.1 nm) at all substrate locations. More importantly, there were no multiple peaks in the normal distribution fit, which suggests that all the thickness values belong to a single distribution. Tukey-Kramer honest significant difference test (Tukey test)[50] was performed to quantitatively determine whether the distributions of the thickness values at the six different substrate locations (shown in Figure 2.4(b)) can be judged as the same distribution. Tukey test is a statistical test that compares multiple distributions simultaneously and shows how different they are from each other, which can be used to categorize similar distributions into separate groups. Figure 2.4(d) is a graphical visualization of the Tukey test results. The comparison circles are shown in Figure 2.4(d) have their centers each aligned with the average thickness values and the radii proportional to the standard deviation values of each distribution. The more the comparison circles overlap, the more similar the distributions are. Here, the comparison circles are all

overlapped and therefore all the distributions can be judged as the same distribution sampled from the same population. Analysis of variance (ANOVA) test[51] was also run to support whether the average values of two or more distributions are statistically identical. Thus, all the average thickness values at each substrate location can be considered statistically identical. To visualize the uniformity in the film thickness over the whole 4-inch wafer, I used a color map to plot the average values of the film thickness at each
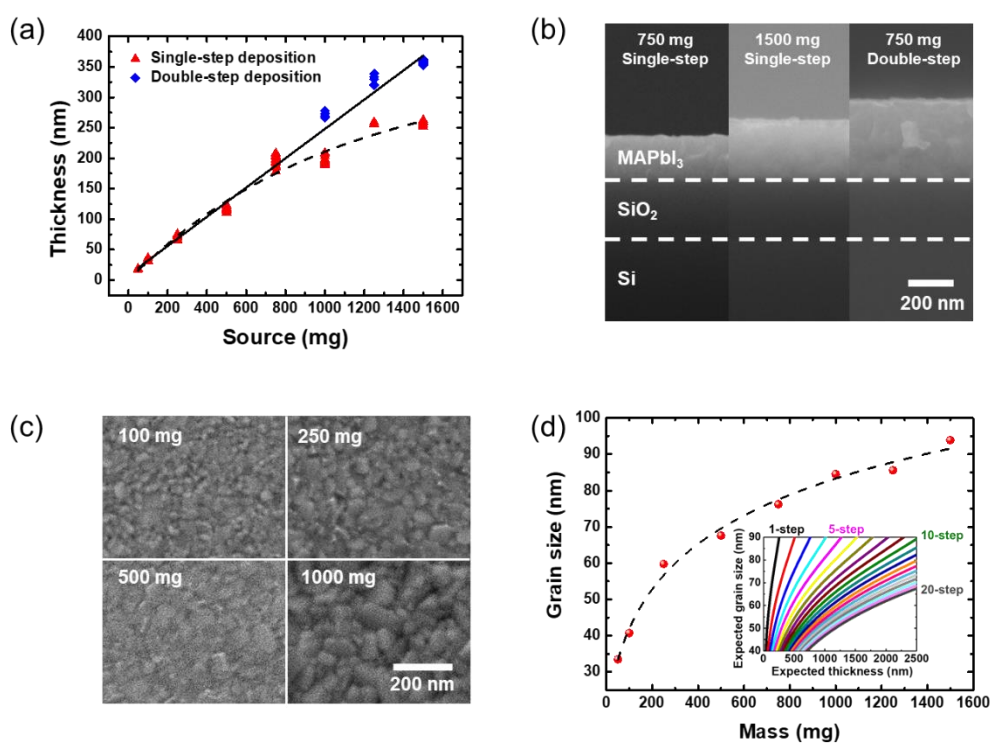
Figure 2.5 (a) A graph of thickness of the flash evaporated perovskite film as a function of the amount of the MAPbI$_3$ single crystal power source. (b) Cross-sectional SEM images for a single- and multi-step deposited perovskite films by flash evaporation for comparison. (c) Top-view SEM images for showing grain size variation for deposition with different source mass. (d) Grain size correlation graph of the deposited perovskite films according to the source mass. The inset shows a predicted controllable range of the grain size and thickness of the MAPbI$_3$ films by the empirical fit shown as the dashed line.

substrate location from A to F (Figure 2.4(e)). The average thickness values at each substrate location differed by less than 2 nm which is smaller than the standard deviation value of 3.1 nm (Figure 2.4(c)). Figure 2.4(f) shows simulation results obtained by the Gaussian process regression with the whole 120 thickness data. The variation of the predicted thickness across the wafer was as small as approximately 2 Å. In addition to the thickness measurement, UV-visible absorbance and PL spectra were measured for the films deposited at each substrate location to confirm that they all have the same absorbance and PL responses regardless of location (see Figure 2.4(g)). All these results consistently support the wafer-scale uniformity of the flash evaporated perovskite film over the 4-inch wafer.

The controllability of the flash evaporation method was demonstrated by depositing various thicknesses of perovskite films by varying the weight of the source materials. The thicknesses of the films were measured by using a cross-sectional FE-SEM as in the uniformity measurement. The thickness increased linearly with increasing the weight of the source from 50 mg to 750 mg (see the red triangle points in Figure 2.5(a)). However, as the weight of the source exceeded 750 mg, the increase in the thickness became sub-linear. In order to mitigate the non-linear relationship above the threshold weight of the source of 750 mg, I introduced a multi-step deposition (i.e. the perovskite films were successively deposited multiple times). For example, to deposit a target thickness of 250 nm, 500 mg of the source perovskite powders were deposited twice (a total of 1000 mg), which could then be described by a linear relationship again (see the blue diamond points in Figure 2.5(a)). Figure 2.5(b) shows the representative cross-sectional SEM images of $MAPbI_3$ films deposited with different weights of the source. Flash evaporation with 1500 mg of the source powders does not yield twice the thickness

of the MAPbI$_3$ film with 750 mg of the source powders. However, successively evaporating 750 mg of the source twice gives a MAPbI$_3$ film twice the thickness (See Figure 2. 5(b)).

I discovered that the grain size could also be controlled by varying the weight of the source powders. The grain size tended to increase as the source mass increased (Figures 2.5(c) and 2.5(d)). I also discovered that the grain size did not vary significantly depending on the number of deposition steps while the thickness increased linearly for a double-step (390 nm) and triple-step (620 nm) evaporated films for the source mass of 750 mg, which potentially provides a way for controlling the grain size independently with the thickness (see the inset of Figure 2.4(d) for the predicted range of grain size for each thickness). The grain size of crystals in perovskite films, along with its thickness, is an important parameter that determines the device performance of optoelectronic devices. In the case of solar cells, the carriers should be able to move freely from the active layer (the point of generation within) to the electrodes (where they are extracted), so the larger the grain, the better the collection efficiency[40]. In the case of LEDs, a higher rate of recombination is desired, and therefore a smaller grain size would be required to fabricate LEDs with higher emission efficiencies[52]. Therefore, our findings can be highly relevant for investigating the relationship between the grain size and device performance of optoelectronic devices based on flash evaporated perovskite films.

In order to demonstrate how the wafer-scale film uniformity discussed so far can be transferred to the uniformity in the optoelectronic device performance, I fabricated photodetectors which are one of the most suitable devices due to their simple structures that require only the deposition of two top contact electrodes on evaporated perovskite films (see the inset of Figure 2.6(a) for the device structure). For performance comparison,
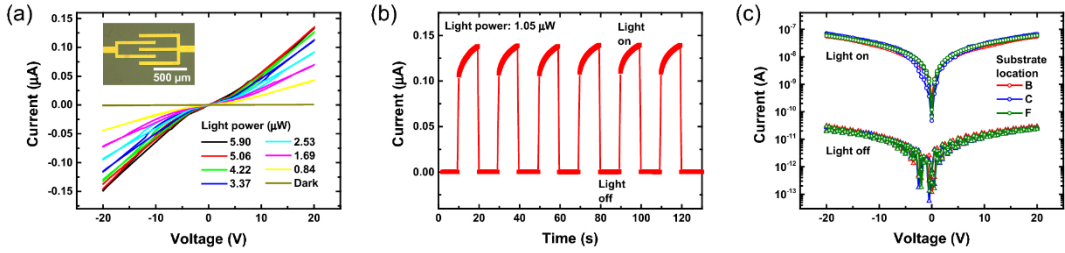
Figure 2.6. Device characteristics of photodetectors prepared by flash evaporation. (a) I-V characteristics under 520 nm laser with different intensities. The inset shows the optical microscope image of the fabricated MAPbI$_3$ photodetector. (b) Time-dependent photoresponse of the photodetector under few cycles of turn-on and off. (c) The I-V characteristics under light and dark conditions for the photodetectors prepared by the flash evaporated films at the different substrate locations.

a photodetector using spin-coated MAPbI$_3$ film was also fabricated. The detailed fabrication process is explained in the Methods section. Figure 2.6(a) shows typical current-voltage curves of the photodetector with the evaporated film under light illumination with 532 nm wavelength and various laser intensities. The photocurrent gradually increased with increasing the laser intensity due to increased photogenerated carrier concentrations. The responsivity (R) which is the ratio of the excess current generated by light illumination to the incident light power was studied. The responsivity decreased as the light power increased. This can be attributed to the increase of carrier-carrier scattering or filling the deep trap states with a longer lifetime, which tends to provide a higher photocurrent at a lower light power[53-55]. The estimated responsivity is 51 mA/W for the photodetector with the flash evaporated film and 137 mA/W for the photodetector with the spin-coated film at a bias of 20 V and light power of 0.84 μW. Detectivity (D*) which is another parameter to characterize the sensitivity of photodetection was calculated according to

$$D^* = R \left(\frac{2eI_{dark}}{A} \right)^{-\frac{1}{2}}$$, where I$_{dark}$ is the dark current, A is the area of the photosensitive region

18

and e is the electric charge. The highest value of detectivity was found to be 9.55×10^{10} Jones within the measured range for the photodetector with the flash evaporated film. This is a comparable value to the detectivity of 1.53×10^{11} Jones for the device with the spin-coated film. These device performance parameters are comparable to the previously reported MAPbI$_3$-based photodetectors[31, 56-58] and commercial Si photodetectors (< 0.2 A/W)[47, 59]. Figure 2.6(b) displays repeated on/off operation of the photodetector with the flash evaporated MAPbI$_3$ film. The device showed relatively fast photo-responses (< 1 s), stable and reproducible operation during the measurement cycles. Finally, in order to demonstrate how the wafer-scale film uniformity discussed above can be transferred to the uniformity in the photodetector device performance, I fabricated photodetectors with flash evaporated films at different locations (see Figure 2.6(c)). The measured device characteristics were nearly identical regardless of the sample substrate locations (B, C, and F), which shows that I can achieve the wafer-scale uniformity in the device performance by our flash evaporation method.

2.3. Experiments

Synthesis of MAPbI$_3$. 2.66 g of PbO and 1.90 g of CH$_3$NH$_3$I (MAI) were dispersed in a mixed acid solution of HI (18 ml, 57 wt% in water) and H$_3$PO$_2$ (2 ml, 50 wt% in water). The solution was heated at 130 °C until all the precursors were dissolved. The solution was then cooled to room temperature to precipitate MAPbI$_3$ single crystals. The crystals were isolated by filtration and dried in vacuum conditions.

Film preparation.

Substrate cleaning. The thermally grown 270 nm thick SiO$_2$ on Si substrate and glass were sequentially cleaned with acetone, 2-propanol, and deionized water in a sonicator for 10

min at each step. SiO$_2$ and glass substrates were exposed to 50 W, 30 sccm condition of O$_2$ plasma for 120 seconds.

Deposition of MAPbI$_3$ film by flash evaporation. Prepared MAPbI$_3$ powder was placed into a tungsten boat. After the pressure in a chamber pumped down to below $1 \cdot 10^{-6}$ Torr, the substrate holder was rotated in 24 rpm for film uniformity, and the current of tungsten boat was rapidly increased to 100 A in 3 seconds. Then, the temperature of the tungsten boat was raised rapidly and MAPbI$_3$ powder sublimated. The nominal deposition rate read by the sensor was approximately 50−80 Å/sec. When the deposition rate decreased to 0.1 Å/sec, the process was terminated and the total deposition time was within 60 seconds.

Deposition of MAPbI$_3$ film by spin-coating. Spin-coating was conducted according to the known hot-casting method[2]. 0.5 M of perovskite precursor solution was prepared by dissolving the prepared MAPbI$_3$ powder in DMF. The cleaned substrate was heated at 120 °C on the hot plate. Then, the heated substrate was quickly moved to the spin-coater and the precursor solution was spin-coated on the substrate for 40 seconds at 5000 rpm.

Fabrication of photodetector. The Au top electrode lines with 50 μm width and 50 nm thickness were deposited using a patterned shadow mask on prepared perovskite film. The electron-beam evaporator pressure was $1 \cdot 10^{-6}$ Torr and the value of the Au deposition rate on the sensor was approximately 1 Å/sec.

Film Characterization.

SEM measurements. The thickness and surface morphology of the perovskite film were analyzed by FE-SEM (JSM-7800F Prime) using an electron beam accelerated at 5 kV for surface morphology study and 10 kV for thickness study.

XRD measurements. Crystallographic structures of perovskite films were analyzed by high resolution X-ray diffraction (HRXRD) technique (Rigaku Smartlab).

Steady-state PL measurements. Steady-state PL spectra of the thin film samples (glass/MAPbI$_3$ film) were measured using a spectrofluorometer (JASCO FP-8500). The excitation wavelength was 520 nm and used Xenon arc lamp (150 W).

Absorbance measurements. The absorbance of the thin film samples (glass/MAPbI$_3$ film) was measured using a UV/Vis spectrophotometer (PerkinElmer LAMBDA 45).

2.4. Conclusions

I designed a single-source flash evaporation setup with a long source-to-substrate distance to deposit MAPbI$_3$ films directly over 4-inch wafer. The thicknesses of the films were measured at various locations of the 4-inch wafer and statistically analyzed to demonstrate that the thicknesses of the films were constant throughout the whole 4-inch wafer. The optical properties of the flash evaporated films were also identical throughout the wafer. The correlation between the amount of the single crystal perovskite powders loaded to the source and the thickness of the deposited film was studied to demonstrate the controllability of the evaporation. I observed that the deposited MAPbI$_3$ film thickness was proportional to the source mass until a critical point, above which the film thickness started to saturate. The proportionality was recovered by introducing the multiple numbers of deposition steps which additionally provided a way for controlling the grain size by varying the source mass and number of deposition steps. The wafer-scale uniformity was preserved for photodetector devices fabricated with flash evaporated MAPbI$_3$ films The fabricated devices showed the responsivity of 51 mA/W and detectivity of 9.55×10^{10} Jones which are comparable to the previously reported MAPbI3-based photodetectors. Our results demonstrate that single-source flash evaporation can be a promising route towards controllably and reliably depositing large-area perovskite films, and therefore producing

perovskite-based optoelectronic devices in large-scale.

References

[1] Zhou H, Chen Q, Li G, Luo S, Song T-b, Duan H-S, Hong Z, You J, Liu Y and Yang Y 2014 *Science* **345** 542-6

[2] Nie W, Tsai H, Asadpour R, Blancon J-C, Neukirch A J, Gupta G, Crochet J J, Chhowalla M, Tretiak S, Alam M A, Wang H-L and Mohite A D 2015 *Science* **347** 522-5

[3] Yang W S, Noh J H, Jeon N J, Kim Y C, Ryu S, Seo J and Seok S I 2015 *Science* **348** 1234-7

[4] Choi H, Mai C-K, Kim H-B, Jeong J, Song S, Bazan G C, Kim J Y and Heeger A J 2015 *Nat. Commun.* **6** 7348

[5] Tsai H, Nie W, Blancon J-C, Stoumpos C C, Asadpour R, Harutyunyan B, Neukirch A J, Verduzco R, Crochet J J, Tretiak S, Pedesseau L, Even J, Alam M A, Gupta G, Lou J, Ajayan P M, Bedzyk M J, Kanatzidis M G and Mohite A D 2016 *Nature* **536** 312-6

[6] Park N-G 2018 *MRS Bull.* **43** 527-33

[7] 2020 NREL. Efficiency chart.

[8] Tan Z-K, Moghaddam R S, Lai M L, Docampo P, Higler R, Deschler F, Price M, Sadhanala A, Pazos L M, Credgington D, Hanusch F, Bein T, Snaith H J and Friend R H 2014 *Nat. Nanotechnol.* **9** 687-92

[9] Zhao X and Tan Z-K 2020 *Nat. Photonics* **14** 215-8

[10] Lee H-D, Kim H, Cho H, Cha W, Hong Y, Kim Y-H, Sadhanala A, Venugopalan V, Kim J S, Choi J W, Lee C-L, Kim D, Yang H, Friend R H and Lee T-W 2019 *Adv. Funct. Mater.* **29** 1901225

[11] Cho H, Jeong S-H, Park M-H, Kim Y-H, Wolf C, Lee C-L, Heo J H, Sadhanala A, Myoung N, Yoo S, Im S H, Friend R H and Lee T-W 2015 *Science* **350** 1222-5

[12] Cao Y, Wang N, Tian H, Guo J, Wei Y, Chen H, Miao Y, Zou W, Pan K, He Y, Cao H, Ke Y, Xu M, Wang Y, Yang M, Du K, Fu Z, Kong D, Dai D, Jin Y, Li G, Li H, Peng Q, Wang J and Huang W 2018 *Nature* **562** 249-53

[13] Fang Y, Dong Q, Shao Y, Yuan Y and Huang J 2015 *Nat. Photonics* **9** 679

[14] Blancon J C, Tsai H, Nie W, Stoumpos C C, Pedesseau L, Katan C, Kepenekian M, Soe C M M, Appavoo K, Sfeir M Y, Tretiak S, Ajayan P M, Kanatzidis M G, Even J, Crochet J J and Mohite A D 2017 *Science* **355** 1288-92

23

[15] Xing G, Mathews N, Lim S S, Yantara N, Liu X, Sabba D, Grätzel M, Mhaisalkar S and Sum T C 2014 *Nat. Mater.* **13** 476-80

[16] Qian L, Sun Y, Wu M, Xie D, Ding L and Shi G 2017 *Adv. Mater.* **29** 1606175

[17] Park N-G 2015 *Mater. Today* **18** 65-72

[18] Yu W, Li F, Yu L, Niazi M R, Zou Y, Corzo D, Basu A, Ma C, Dey S, Tietze M L, Buttner U, Wang X, Wang Z, Hedhili M N, Guo C, Wu T and Amassian A 2018 *Nat. Commun.* **9** 5354

[19] Momblona C, Gil-Escrig L, Bandiello E, Hutter E M, Sessolo M, Lederer K, Blochwitz-Nimoth J and Bolink H J 2016 *Energy Environ. Sci.* **9** 3456-63

[20] Mitzi D B, Prikas M T and Chondroudis K 1999 *Chem. Mater.* **11** 542-4

[21] Niu L, Liu X, Cong C, Wu C, Wu D, Chang T R, Wang H, Zeng Q, Zhou J, Wang X, Fu W, Yu P, Fu Q, Najmaei S, Zhang Z, Yakobson B I, Tay B K, Zhou W, Jeng H T, Lin H, Sum T C, Jin C, He H, Yu T and Liu Z 2015 *Adv. Mater.* **27** 7800-8

[22] Lan C, Dong R, Zhou Z, Shu L, Li D, Yip S and Ho J C 2017 *Adv. Mater.* **29** 1702759

[23] Chen Y, Zhang L, Zhang Y, Gao H and Yan H 2018 *RSC Adv.* **8** 10489-508

[24] Jeon N J, Noh J H, Kim Y C, Yang W S, Ryu S and Seok S I 2014 *Nat. Mater.* **13** 897-903

[25] Wu T, Wu J, Tu Y, He X, Lan Z, Huang M and Lin J 2017 *J. Power Sources* **365** 1-6

[26] Burschka J, Pellet N, Moon S-J, Humphry-Baker R, Gao P, Nazeeruddin M K and Grätzel M 2013 *Nature* **499** 316-9

[27] Im J-H, Jang I-H, Pellet N, Grätzel M and Park N-G 2014 *Nat. Nanotechnol.* **9** 927-32

[28] Ávila J, Momblona C, Boix P P, Sessolo M and Bolink H J 2017 *Joule* **1** 431-42

[29] Li G, Ho J Y L, Wong M and Kwok H-S 2016 *physica status solidi (RRL) – Rapid Research Letters* **10** 153-7

[30] Crane M J, Kroupa D M, Roh J Y, Anderson R T, Smith M D and Gamelin D R 2019 *ACS Applied Energy Materials* **2** 4560-5

[31] Wei H, Ma H, Tai M, Wei Y, Li D, Zhao X, Lin H, Fan S and Jiang K 2017 *RSC Adv.* **7** 34795-800

[32] Liu M, Johnston M B and Snaith H J 2013 *Nature* **501** 395-8

[33] Yang D, Yang Z, Qin W, Zhang Y, Liu S and Li C 2015 *J. Mater. Chem. A* **3** 9401-5

[34] Chen C-W, Kang H-W, Hsiao S-Y, Yang P-F, Chiang K-M and Lin H-W 2014 *Adv. Mater.* **26** 6647-52

[35] Bohee H and Jang-Sik L 2017 *Adv. Mater.* **29** 1701048

[36] Ono L K, Wang S, Kato Y, Raga S R and Qi Y 2014 *Energy Environ. Sci.* **7** 3989-93

[37] Hwang B and Lee J-S 2018 *Adv. Opt. Mater.* **7** 1801356

[38] Tai M, Zhao X, Wei H, Wang G, Hao F, Li X, Yin X, Zhou Y, Han J, Wei Y, Jiang K and Lin H 2018 *ACS Appl. Mater. Interfaces* **10** 26206-12

[39] Wei H, Zhao X, Wei Y, Ma H, Li D, Chen G, Lin H, Fan S and Jiang K 2017 *NPG Asia Mater.* **9** e395-e

[40] Xu H, Wu Y, Xu F, Zhu J, Ni C, Wang W, Hong F, Xu R, Xu F, Huang J and Wang L 2016 *RSC Adv.* **6** 48851-7

[41] Longo G, Gil-Escrig L, Degen M J, Sessolo M and Bolink H J 2015 *Chem. Commun.* **51** 7376-8

[42] Kim H-S, Lee C-R, Im J-H, Lee K-B, Moehl T, Marchioro A, Moon S-J, Humphry-Baker R, Yum J-H, Moser J E, Grätzel M and Park N-G 2012 *Sci. Rep.* **2** 591

[43] Momblona C, Malinkiewicz O, Roldán-Carmona C, Soriano A, Gil-Escrig L, Bandiello E, Scheepers M, Edri E and Bolink H J 2014 *APL Mater.* **2** 081504

[44] Zhao L, Lee K M, Roh K, Khan S U Z and Rand B P 2019 *Adv. Mater.* **31** 1805836

[45] Huang C-Y, Wu C-C, Wu C-L and Lin C-W 2019 *ACS Omega* **4** 8081-6

[46] Climent-Pascual E, Hames B C, Moreno-Ramírez J S, Álvarez A L, Juarez-Perez E J, Mas-Marza E, Mora-Seró I, de Andrés A and Coya C 2016 *J. Mater. Chem. A* **4** 18153-63

[47] Wang K, Wu C, Yang D, Jiang Y and Priya S 2018 *ACS Nano* **12** 4919-29

[48] Saidaminov M I, Abdelhady A L, Murali B, Alarousu E, Burlakov V M, Peng W, Dursun I, Wang L, He Y, Maculan G, Goriely A, Wu T, Mohammed O F and Bakr O M 2015 *Nat. Commun.* **6** 7586

[49] Kong W, Ye Z, Qi Z, Zhang B, Wang M, Rahimi-Iman A and Wu H 2015 *Phys. Chem. Chem. Phys.* **17** 16405-11

[50] Tukey J W 1977 *Exploratory data analysis* vol 2: Reading, Mass.)

[51] Scheffe H 1999 *The analysis of variance* vol 72: John Wiley & Sons)

[52] Yuan M, Quan L N, Comin R, Walters G, Sabatini R, Voznyy O, Hoogland S, Zhao Y, Beauregard E M, Kanjanaboos P, Lu Z, Kim D H and Sargent E H 2016 *Nat. Nanotechnol.* **11** 872-7

[53] Zhang W, Huang J-K, Chen C-H, Chang Y-H, Cheng Y-J and Li L-J 2013 *Adv. Mater.* **25** 3456-61

[54] Konstantatos G, Howard I, Fischer A, Hoogland S, Clifford J, Klem E, Levina L and Sargent E H 2006 *Nature* **442** 180-3

[55] Konstantatos G, Clifford J, Levina L and Sargent E H 2007 *Nat. Photonics* **1** 531-4

[56] Bao C, Zhu W, Yang J, Li F, Gu S, Wang Y, Yu T, Zhu J, Zhou Y and Zou Z 2016 *ACS Appl. Mater. Interfaces* **8** 23868-75

[57] Gegevičius R, Treideris M, Pakštas V, Franckevičius M and Gulbinas V 2018 *Adv. Electron. Mater.* **4** 1800114

[58] Bai F, Qi J, Li F, Fang Y, Han W, Wu H and Zhang Y 2018 *Adv. Mater. Interfaces* **5** 1701275

[59] Guo F, Yang B, Yuan Y, Xiao Z, Dong Q, Bi Y and Huang J 2012 *Nat. Nanotechnol.* **7** 798-802

Chapter 3. Tailored Design-of-Experiments Approach for Optimization of Flash-Evaporated Organic Inorganic Halide Perovskite-based

In this thesis, I described optimization method of flash-evaporation to deposit perovskite films. Single-source flash evaporation method has recently gained attention for its potential as a rapid and solvent-free deposition method for producing organic-inorganic halide perovskite (OHP) films in large-scale. However, due to a complex nature of the different experimental parameters involved in the deposition process, it is not straightforward to obtain the optimal condition for producing high-quality OHP films. In this study, I tackle this problem by employing the design-of-experiment (DOE) process, which is an efficient statistical analysis for finding an optimized condition with a minimized number of experiments. The DOE process was used for optimizing the responsivity of the OHP photodetector devices against the input variables used in the deposition that yielded an enhanced responsivity of 112.2 mA/W, which is up to an order of magnitude higher than that of the unoptimized devices. Our experimental results using the DOE method provide not only the conditions required for enhancing the device performance but also the guidelines for improving the overall film quality through exploring the variable space of the flash evaporation technique.

3.1. Introduction

Organic-inorganic halide perovskites (OHPs) have recently received enormous attention due to their excellent properties for optoelectronic[1-17] and electronic[18-21] devices. Out of various deposition methods studied in the field, solution-processing[7, 22, 23], chemical vapor deposition (CVD)[24, 25] and thermal evaporation[26, 27] have gained the most attention for OHPs. Spin-coating techniques of OHPs are mainly used in lab-scale device fabrication because it is a low-cost and easily accessible process. Although

some works have reported remarkable device performances in large-area perovskite optoelectronic devices made with spin-coated perovskite films,[12, 28] the spin-coating techniques face a challenge in producing reliable and uniform films over a large area. On the other hand, evaporation methods, which include dual-source vacuum deposition, sequential-partial pressure, mixed solution and vapor deposition, modified chemical vapor deposition method and single-source deposition, have shown a potential for producing uniform films over a large area.[29, 30] The evaporation methods do not require the use of solvents and thus have the advantage that the films can be deposited without solvent-induced-damages which are critical for organo-metal-halide perovskite films.[31, 32] Organo-halide precursor (e.g. methylammonium iodide, MAI) and lead-source precursor (e.g. lead iodide, PbI_2) can be thermally evaporated by various methods, i.e., co-evaporation method,[26, 33, 34] vapor-assisted deposition[1, 35] or sequential deposition[36-38] to fabricate OHP (e.g. methylammonium lead iodide, $MAPbI_3$) films. Although these deposition methods are well-established, it is crucial to produce OHP films with the desired stoichiometric ratio among the three different ionic components by evaporation because each precursor has different sublimation temperatures.[30]

The single-source flash evaporation method[27, 32, 39-41] has gained attention as a candidate for thermally evaporating from either a mixed-precursor source or pre-synthesized stoichiometric OHP source by expeditiously raising the temperature in a short time. In principle, the rapid vaporization of the single crystal precursors results in a uniform and homogeneous evaporation of the precursors while maintaining the same ratio between the different components in OHP.[32] Furthermore, the single-source flash evaporation method can be expanded to fabricate OHP films with mixed cation and halide species, which is challenging in other methods.[30] Although these aspects of the single-source

28

flash evaporation present potential of exploring a diverse compositional range of OHPs, there has been relatively few reports which have systematically studied the film quality optimization by considering the relationship between relevant input and response variables of the flash evaporation method.

The one-factor-at-a-time (OFAT) method, which is commonly used as a systematic experimental method, has clear disadvantages that it is relatively time-consuming and does not consider interaction effects because only one input variable is considered at a time. Moreover, most of the experimental designs typically require a long time to gather a sufficiently large training data set. Even after the model is completed, precise data predictions are limited to the variables within the range of the training data set. In this way, the effects of single input variables, e.g., substrate temperature,[42] excess amount of MAI, and chamber pressure[41] on the resulting film quality of the evaporated OHP films have been previously studied by following the OFAT method. However, multi-variable interactions and correlations between the input and response variables for achieving desired film properties have not yet been investigated, to the best of our knowledge.

On the contrary, the design-of-experiment (DOE) approach[43, 44] is a multivariate statistical method that is optimized for minimal experimentation. In addition, the DOE method allows us to consider the correlation between the variables in the analysis step and discover optimal experimental conditions via regression analysis. Because the DOE approach considers various variables simultaneously, it is an efficient tool for achieving experimental targets in a relatively short period of time, given that a clear objective is set. Although the DOE approach remains as a powerful tool for performing multivariate statistical analysis, it has been rarely used for investigating the film deposition conditions of organo-metal-halide perovskites.[45]

In our study, the DOE approach was used to analyze the relationship between the variables that affect the film deposition in the flash evaporation method, which in turn, provided guidelines for optimizing the deposition conditions that produce high-quality perovskite films with the desired optoelectronic properties. Our developed flash evaporation method was recently shown to be highly reproducible and only had few control variables, both of which are suitable for employing the DOE approach for optimizing the film quality. In the analysis process, I first investigated the input variables that affect the physical and optoelectronic properties of the deposited perovskite films and extracted the relationships between these properties. By extending the film characterizations to photodetector devices, the DOE method was able to predict the responsivity values, which allowed us to design devices with a high responsivity value that was up to an order of magnitude higher than that of the devices fabricated from off-optimum conditions.

3.2. Result and Discussion

The overall stages of DOE method can be best described as sequential procedures that consist of 1) planning the experiments, 2) executing the experiments, 3) analyzing the results, and 4) optimizing via data analysis. In the stage of planning the experiments, input variables, response variables and experimental design are chosen according to the set objective. In this study, I employed response surface method (RSM) out of various experimental which is suited for optimizing deposition conditions for producing high-quality flash-evaporated $MAPbI_3$ films.[46, 47] Among the RSM designs, the Box-Behnken design was chosen because it is an efficient design that needs relatively few numbers of experiments for optimization. It acquires data that correspond to experiments at the center of each side of the cubic variable space[48] (see Figure 3.1(a)). The length of
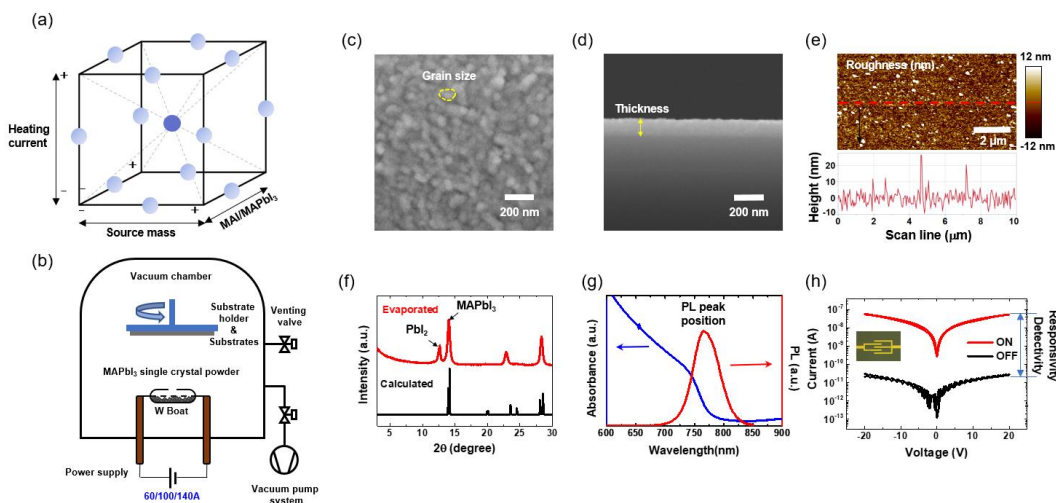
30

Figure 3.1. (a) A graphical representation of the Box-Behnken design for three factors (heating current, source mass, and excess MAI ratio). (b) A schematic illustration of single-source flash evaporation to deposit a MAPbI$_3$ film. (c) surface and (d) cross-sectional SEM images, and (e) an AFM image of the flash-evaporated MAPbI$_3$ film. (f) X-ray diffraction pattern of the flash-evaporated MAPbI$_3$ film (red) and calculated data (black) from the unit cell of MAPbI$_3$. (g) UV-visible absorbance spectra (blue) and PL spectra (red) of the MAPbI$_3$ film (h) I-V characteristics of flash-evaporated perovskite photodetectors under white light illumination (red) and dark (black) conditions, which were used to extract responsivity (R) and specific detectivity ($D*$).

each side of the cube represents a range of input variables and each point at the center (represented as circles in Figure 3.1(a)) corresponds to a set of input variables (i.e. an experimental condition) used for each experiment. In the Box-Behnken design, when three input variables are selected, 13 different experimental conditions are determined, and the center point experiment condition (dark blue circle in Figure 3.1(a)) is repeatedly evaluated three times to verify reproducibility and robustness of the model. By using such an experimental model, the experiments are arranged regularly such that potential bias towards specific experimental conditions is avoided. Therefore, it is a convenient model to analyze

the effect of individual input variables on each response variable, as well as the interactions between them.

The objective of the DOE process was to find the optimal deposition condition for single-source flash evaporation of MAPbI$_3$ film (from the set-up schematically drawn in Figure 3.1(b)) that results in high-performance photodetectors. In total, three input variables were selected based on the previous studies on flash evaporation of OHP films. An excess amount of MAI added to the source (i.e. an excess molar ratio of MAI to MAPbI$_3$ powder) was selected as the first variable because it has been reported to play a role in reducing PbI$_2$ impurity in the evaporated film which is related to the relative purity of the evaporated film.[41] The other input variables were the mass of MAPbI$_3$ single crystal source (source mass, the second variable) and the heating current (related to the heating temperature, the third variable) which control the total amount of evaporated materials and sublimation rate, both of which affect the thickness and grain size of the deposited MAPbI$_3$ films. By combining these three input variables that control the relative purity, grain size, and thickness of the MAPbI$_3$ films, I attempted to find out the relationships between physical properties, optoelectronic properties, and the resulting device performance of photodetectors made with the flash-evaporated MAPbI$_3$ films.

In the DOE process, the selection of the evaluation scope, which is expressed as the size of the variable cube shown in Figure 3.1(a), is important because I can extract the effect of multi-input-variables on each response variable, and thus find out optimum experimental condition within the evaluated range of the variables. The range of the input variables should be selected such that it is neither too wide to prevent an accurate linear regression analysis nor too narrow to risk the loss of generality of the extracted model. As a 1:1 molar ratio between MAI and MAPbI$_3$ was found to be ideal for reducing PbI$_2$

32

impurity in a previous study,[41] the evaluation range was selected from 0.5 to 1.5 mol ratio. In order to control the range of thickness from 500 to 2000 Å, the source mass (the second variable) was evaluated in the range from 250 to 750 mg. For the heating current (the third variable), 60 A represented a slow sublimation of the source, nearly approaching the rate of conventional thermal evaporation. Therefore, the heating current was evaluated in the range between 60 A and 140 A. In order to find out the effect of the aforementioned input variables, various physical and optoelectronic properties were measured. The measured properties were chosen as the response variables used to perform the multivariate analysis. The selected response variables are various film properties: grain size, thickness, roughness, relative purity, and photoluminescence (PL) peak position and photodetector device properties: responsivity and specific detectivity (Figures 3.1(c)-(h)).

Here, I show how I characterized each response variable by outlining the results for the evaporated film under the central condition, defined by the variable coordinate of 500 mg (source mass), 100 A (heating current), and 1.0 mol ratio (excess MAI ratio). Firstly, the structural properties were probed by microscopy and X-ray diffraction (XRD) measurements. The resulting evaporated $MAPbI_3$ film had a grain size of approximately 37 nm (σ : 7.2 nm) and a thickness of 133.3 nm (σ : 3.8 nm) as determined from the top-surface image and cross-sectional image measured with field-emission scanning electron microscope (FE-SEM) (Figures 3.1(c) and (d)). The grain size and thickness were averaged after measuring 20 locations in an image. The surface morphology of the film was probed by measuring the root-mean-squared value of surface roughness (Rq), which was measured to be 1.8 nm by atomic force microscope (AFM) (Figure 3.1(e)). Next, we used XRD data to determine the relative purity. Before discussing the relative purity, please note that the XRD data show good crystallinity of the $MAPbI_3$ film. XRD data showed peaks at 14.0

and 28.0 degrees (2θ) that coincide with (110) and (220) diffraction peaks of the predicted MAPbI$_3$ results (Figure 3.1(f)). The crystallinity of the film was analyzed by XRD data which showed peaks at 14.0 and 28.0 degrees (2θ) that coincide with the predicted results (Figure 3.1(f)). In addition, to determine the relative purity of the film, Rietveld refinement[49-51] was used to quantitatively estimate the amount of PbI$_2$ present in the MAPbI$_3$ film from the XRD data. Since the ratio of PbI$_2$ in the MAPbI$_3$ film is proportional to the XRD peak intensity, I defined the relative purity of the films with the following formula,

$$Relative\ purity = \ln\left(\frac{I_{MAPbI_3}\ (14.0°)}{I_{PbI_2}\ (12.6°)}\right),$$

where I_{MAPbI_3} (14.0°) and I_{PbI_2} (12.6°) represent the XRD peak intensity at 14.0° and 12.6° that correspond to MAPbI$_3$ and PbI$_2$, respectively. Secondly, the photophysical properties of the MAPbI$_3$ film were measured by PL and UV-Vis absorbance spectra to determine the wavelengths of the emission peak and absorption edge, respectively. The PL peak position appeared at near 765 nm which is identical to the expected results from previous studies[39, 52, 53] and UV-vis absorbance edge appeared at 758 nm (Figure 3.1(g)).

Two of the most important response variables of interest can be the device performance parameters of the photodetectors fabricated with the flash-evaporated MAPbI$_3$ film. They are the responsivity (R) which represents a quantitative measure of how much excess electrical current output comes out when illuminated with light input and specific detectivity (D^*) corresponding to the magnitude of the signal to noise ratio of a photodetector per unit bandwidth and unit area. In detail, the responsivity and specific detectivity are determined by $R = (I_{light} - I_{dark})/(PA)$ and $D^* = R\left(\frac{A}{2eI_{dark}}\right)^{\frac{1}{2}}$,

respectively, where I_{light} is the current under illumination, I_{dark} is the dark current, P is the light intensity, A is the area of photosensitive region of the OHPs film, and e is the electric charge.[17, 54, 55] The calculated responsivity of the device made with the film deposited under the central condition was found to be 57.8 mA/W (σ : 8.4 mA/W) (at the applied voltage of 20 V and incident light power of 667 µW) and the specific detectivity was found to be 1.8×10^9 Jones (σ : 4.6×10^{10} Jones).
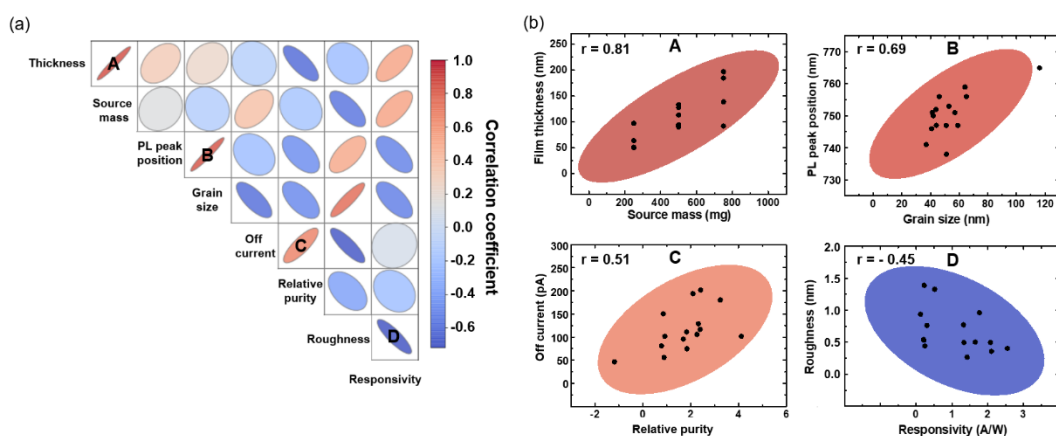

Figure 3.2 (a) Multi-variable correlation matrix plot. (b) Representative correlation graphs for source mass and film thickness, grain size and PL peak position, relative purity and off current, and responsivity and surface roughness. The ellipses in the graphs show the regions with the confidence level of 90 %.

I now explain how the response variables mentioned above were analyzed via the DOE approach to study the correlation between each structural and photophysical property of the evaporated films, which later can be related to the device performances. A total of 15 experiments were conducted with 13 different types of perovskite films made for each condition specified in Figure 3.1(a). Before the regression analysis was conducted, the correlation matrix plot was used to understand the correlation between the variables, which were quantitatively estimated through the value of correlations (Figure 3.2(a)). The

35

correlation matrix plot which is a set of scattering plots between variables provides a simple and holistic approach to check the relationships between the variables before performing detailed regression analysis. The correlations were analyzed by extracting the density ellipse for pairs of each input and response variable. The density ellipse displays the area that contains 90% of the total data in Figure 3.2(b). When 13 numerical variables were analyzed by the correlation matrix plot, the correlation matrix plot in Figure 3.2(a), which consists of 8 variables, could be expressed to focus on a set of variables with a significant degree of correlation. The following four correlation results were aligned with our expectations: the thickness of the deposited film increased as the source mass increased, as expected (plot A in Figure 3.2(b)). The wavelength of the PL peak position increased as the grain size increased (plot B in Figure 3.2(b)). This red-shift in the PL emission as larger grain size is related to photon-reabsorption of emitted light in larger crystal grains, as reported previously.[56] The higher the relative purity, the larger the dark (off) current (plot C in Figure 3.2(b)), which is related to PbI_2 acting as a charge-intercept barrier[57] (i.e. the dark current increased as the relative proportion of PbI_2 decreased). The responsivity decreased when the film surface became rougher (plot D in Figure 3.2(b)). A smooth morphology is likely to improve the charge transport which can lead to improved photoconductive gain, and therefore a larger photocurrent.[58] Although there is no absolute standard for the correlation coefficient (r) categorization, the r value falling within the range between 0.68 and 1.0 (plot A and B in our case) can be generally considered to indicate a strong correlation, and the range between 0.36 and 0.67 (plot C and D in our case) a moderate correlation.[59]

There were nontrivial correlation results that could be identified with the correlation analysis such as relatively strong correlations between heating current versus off current

(+, positive correlation), PL intensity versus thickness (+), grain size versus roughness (+), and PL intensity versus responsivity (+) and the weak correlations between excess MAI ratio versus thickness, MAI ratio versus grain size, relative purity versus responsivity, and relative purity versus specific detectivity. Although some of these weak correlation results were unexpected (e.g. excess MAI ratio versus thickness/grain size and relative purity versus responsivity/specific detectivity), I could build upon these simple correlation analyses to examine the most relevant factors for optimizing the photodetector device performance parameters by performing detailed regression analyses.

Before going into the regression analysis step, it is necessary to verify the reproducibility of the results to confirm the robustness of the experimental environment. I checked the reproducibility by comparing the three experiments performed for the central condition and re-evaluated additional conditions in the DOE cube. The data clearly show the reproducibility of the thickness, grain size, relative purity, and responsivity under the central condition and an additional DOE Condition. The DOE approach, which analyzes data from multiple angles, can reduce misinterpretation by considering the interactions that can be overlooked in the optimizing process by OFAT method. Through regression analysis, each response variable can be quantitatively associated as a function of input variables to derive meaningful relationships between various film properties and device performance.[60] The regression analysis was performed on 7 response variables-grain size, thickness, roughness, relative purity, PL peak position, responsivity, and specific detectivity- which revealed that grain size, thickness, relative purity, and responsivity values could be modeled well with input variables. On the other hand, the accuracy of modeling roughness, PL peak position, and specific detectivity was relatively low, and therefore these variables were excluded from the subsequent analysis.

For each response variable, I can represent the regression model as a three-dimensional (3D) scattering plot with the axes and range corresponding to the input variable cube shown in Figure 3.1(a). In the case of the thickness (Figure 3.3(a)), if I examine a cross-section from the 3D scattering plot perpendicularly to the excess MAI ratio axis at MAI/MAPbI$_3$ ratio of 1 (shown as the brown dashed line in Figure 3.3(a)), a two-dimensional (2D) contour plot can be extracted with the source mass and heating current (Figure 3.3(b)). If I look closely at the lines along with the heating current values of 60 A (green line in Figure 3.3(b)), 100 A (orange), and 140 A (black), the thickness increases linearly with the source mass for all the current values (Figure 3.3(c)). However, the slope
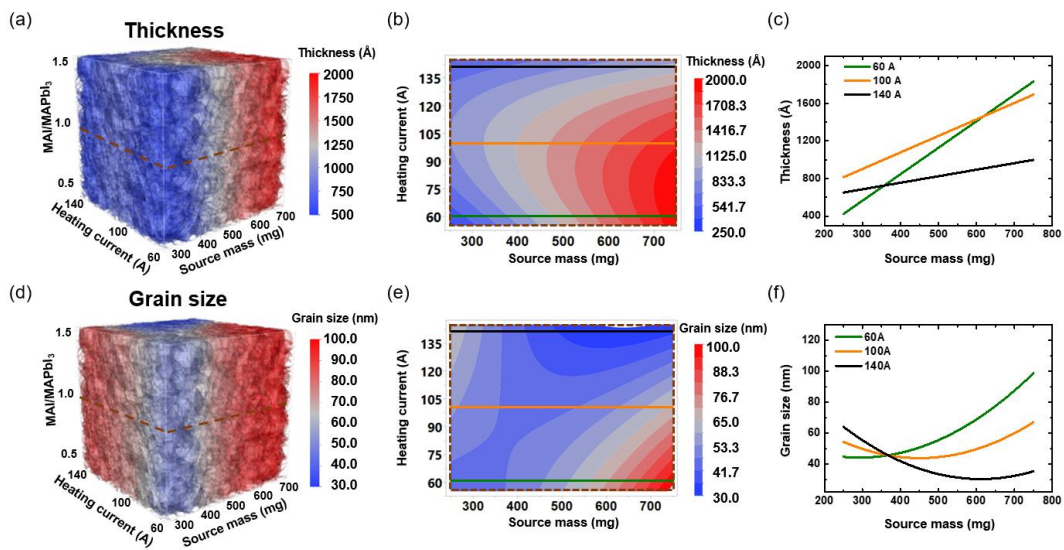

Figure 3.3 (a) A 3D scattering plot of the film thickness according to the heating current, source mass, and excess MAI ratio (MAI/MAPbI$_3$) from the regression analysis. (b) A contour plot of the film thickness according to the heating current and the source mass. (c) Graphs of the film thickness as a function of the source mass at the different heating currents of 60 A (green line), 100 A (orange line), and 140 A (black line). (d), (e), and (f) are the same graphs as (a), (b) and (c) but represent the grain size instead of the film thickness.

38

of the increase in the thickness varies according to the heating current: the lower the heating current, the larger the slope. This is an example of an interaction effect, where the effect of one input variable (i.e. source mass) on a response variable (i.e. thickness) depends on another variable (i.e. heating current).

The regression analysis for grain size (Figure 3.3(d)) reveals the feature of interaction effect more clearly. I can no longer observe simple linear relationships between the source mass and the grain size in the 2D contour plot at an excess MAI ratio of 1 (Figures 3.3(e) and (f)). Depending on the heating current, the grain size either increases (heating current of 60 A) or decreases (140 A) with source mass. This is a good example of an interaction effect, where a response variable (i.e. grain size) is affected strongly by interaction terms of multiple variables (i.e. heating current × source mass). In other words, the grain size cannot be represented by a simple linear model. This is the origin of an apparently weak correlation between the grain size and the source mass from the correlation matrix plot in Figure 3.2, since the interaction with other variables (i.e. heating current) was neglected. Similarly, each interaction between input variables for each response variable can be effectively expressed by the interaction plot. Overall, I have demonstrated that the multivariate regression analysis allows us to predict various film properties by modeling their complex relationships with multiple input variables which collectively define the film deposition conditions.

The goal of our study is to employ DOE for optimizing film deposition conditions for obtaining high-performance flash-evaporated perovskite photodetector devices. The DOE process allowed us to predict the responsivity values of photodetector devices via regression analysis as can be shown from a high R^2 value. In order to optimize the responsivity, the deposition condition can be simply found where the predicted responsivity

value reaches maximum in the regression analysis result. In this way, it is possible to fabricate photodetectors with film deposition conditions predicted to achieve the maximum responsivity value without individually controlling the factors that affect responsivity such as grain size, relative purity, and trap density. Nevertheless, it is informative to carry out a detailed correlation analysis in order to find out the main factors accountable for the optimized device performance. Therefore, I focused on extracting relationships between responsivity and other response variables for which reliable regression models with high R^2 values were obtained: thickness, relative purity, and grain size.
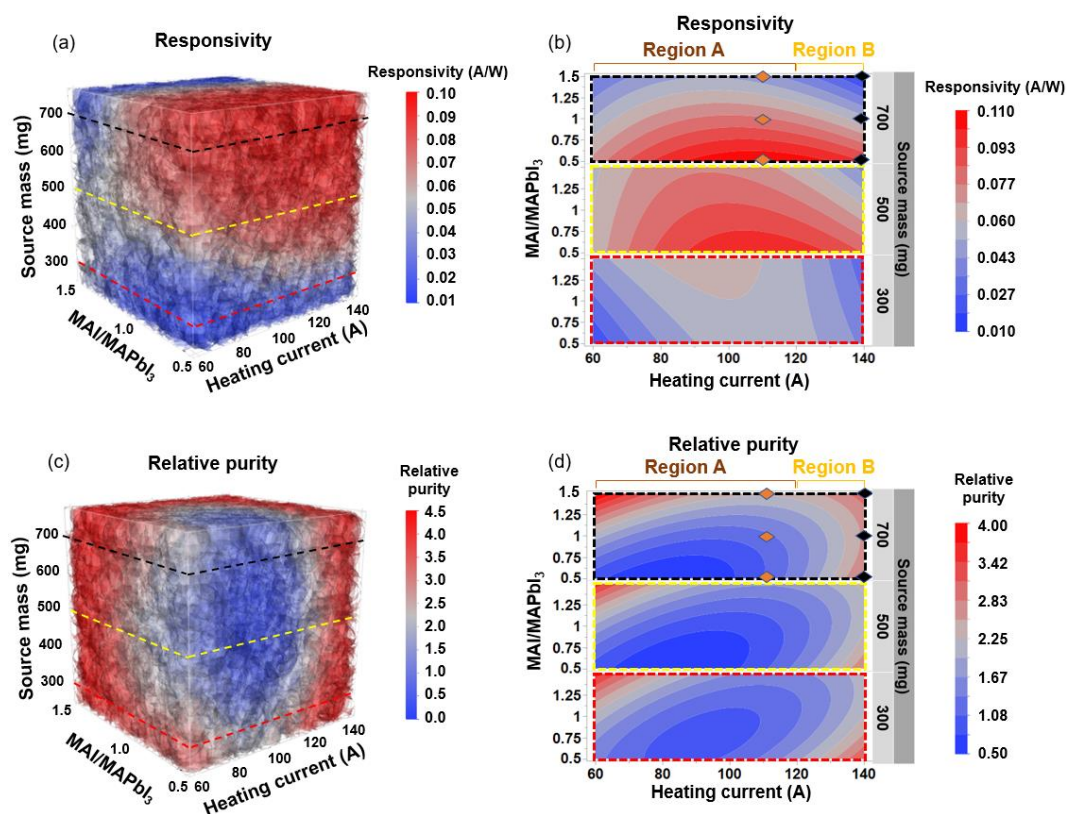

Figure 3.4. 3D scattering plots of (a) the responsivity and (c) the relative purity according to the heating current, source mass, and MAI/MAPbI$_3$ from the regression analysis. Contour plots of (b) responsivity and (d) the relative purity is extracted from 3D scattering data (Figure 3.4(a) and (c)) at the source mass of 300, 500, 700 mg.

As shown in the 3D scattering plot (Figure 3.4(a)), the responsivity is predicted to increase as the source mass increases. This is expected due to the strong influence of the source mass on the deposited thickness of the perovskite film (Figure 3.3(c)). Since the tested thickness range is significantly smaller than the expected light penetration depth in MAPbI$_3$,[61] the generated photocurrent at the same input light power will attune to a similar scale with the thickness of the film. I have experimentally confirmed the thickness scaling in the responsivity by comparing photodetector devices made with multi-stacked perovskite films.

I tried to discover hidden details within the expected thickness scaling of the responsivity by looking at 2D contour plots (Figure 3.4(b)) generated from planar cross-sections of the 3D plot for the source mass of 300 mg (red dashed line cut in Figure 3.4(a)), 500 (yellow), and 700 mg (black). Figures 3.4(c) and (d) are the 3D scattering plots and corresponding 2D contour plots generated from the regression analysis for the relative purity of the evaporated film. When comparing Figures 3.4(b) and (d) as a whole, the responsivity and relative purity do not seem to have a clear correlation, which implies complexities in relating the responsivity and relative purity from the input variables. However, when it comes to a smaller deposition condition range, a noticeable correlation can be found. More specifically, if I divide the regions according to the heating current value as "Region A" from 60 A to 120 A and "Region B" from 120 A to 140 A (see Figures 3.4(b) and (d)), a negative correlation between responsivity and relative purity can be seen in Region A in the contour plot for the source mass of 700 mg (top panels of Figures 3.4(b) and (d)). This result is consistent with previous reports that the responsivity increases with incorporation of PbI$_2$ impurities in the perovskite film.[57, 62-64] The origin of the different trends between the responsivity and relative purity in Region B is not entirely

clear, but a finite formation of extra perovskite phases such as low dimensional perovskites[52] by evaporating films at the high heating current values near 140 A may contribute to the discrepancy. The grain size and responsivity showed a relatively small correlation, which may be due to a limited range of the grain size tested in our study compared to previous works.[65]

In order to experimentally confirm our regression models with actual data, I fabricated photodetectors with perovskite films evaporated under six deposition conditions at the edge of Region A and Region B (the orange and black points in Figures 3.4(b) and (d)). Firstly, for the three conditions denoted as the orange points in Region A, I could confirm the negative correlation between the relative purity and the responsivity, as predicted by the regression analysis, i.e., the relative purity increased and responsivity decreased as increasing the excess MAI ratio.

In addition, I further investigated the origin of the negative correlation between the relative purity of the evaporated film and the responsivity from the films deposited at these three conditions: a low relative purity film seems to contain some PbI_2 on the surface of the perovskite film suppressing non-radiative recombination near the contacts[57, 62-64]. Secondly, for the other three deposition conditions denoted as black points in Region B, the relative purity of the film remained relatively constant but the responsivity decreased with the excess MAI ratio (Figure 3.4(b)), which also confirms the predictions from the regression model. The sound agreements between the experimental results for the responsivity and relative purity with the prediction of the regression models guarantee the reliability of the formulated regression models.
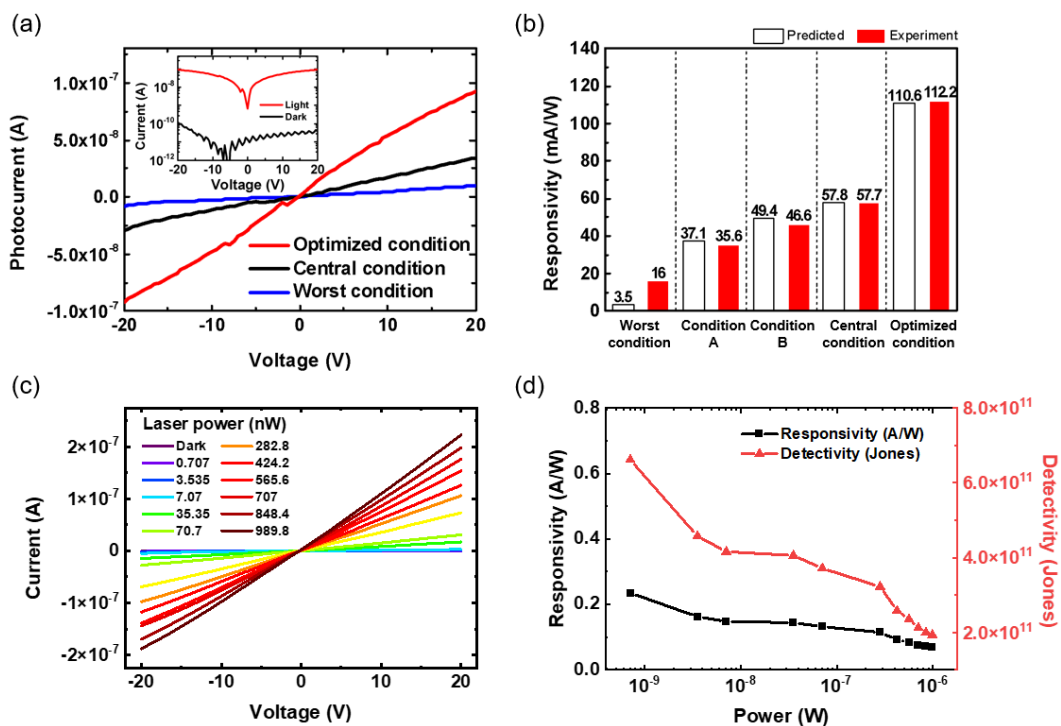
Figure 3.5 (a) I-V characteristics of white light illuminated photodetectors with three different MAPbI$_3$ films which are flash-evaporated under the optimized (red), central (black), and worst (blue) deposition condition. The inset shows log-scale I-V curves of the optimized photodetector under white light illumination (red) and dark (black) conditions. (b) The predicted responsivity values from the regression model (white) and experimental values (red) under various deposition conditions. Device characteristics of the photodetectors prepared by the optimized deposition conditions. (c) I-V characteristics under 520 nm laser illumination with different intensities. (d) Photoresponsivity and detectivity of the flash evaporated MAPbI$_3$ photodetectors operated at a bias voltage of 20 V as a function of the incident laser power, both of which decrease with power, as expected.

As the final step of the DOE process, I fabricated a photodetector device with the optimized film deposition condition and evaluated its device performance. The optimized deposition condition for maximizing the responsivity was predicted to the source mass of

650 mg, the excess MAI mol ratio of 0.5, and the heating current of 110 A. For comparison, other photodetectors were also fabricated with perovskite films deposited under the conditions expected to perform worse: including the predicted worst deposition condition (the source mass of 750 mg, the excess MAI mol ratio of 1.5, and the heating current of 140 A). Figure 3.5(a) shows the photoelectric characteristics of photodetectors made of the perovskite films deposited under several different deposition conditions including the optimized and the worst condition. As expected, the photocurrent was largest in the optimized photodetector and smallest in the worst condition photodetector. The responsivity of the optimized device was found to be 112.2 mA/W (σ : 20.6 mA/W), as confirmed from multiple evaluations. This is a 98% improvement over the responsivity of the central condition photodetector, and 600% improvement over that of the worst condition photodetector. Moreover, to confirm the aforementioned influence of PbI_2 on the photodetector performance, approximately 0.3% of PbI_2 was detected in the deposited film via Rietveld refinement of the X-ray diffraction pattern.

Although the specific detectivity values of photodetector devices were not discussed previously due to low reliability of the regression model, the specific detectivity could be also significantly improved with the value for the optimized device showing an order of magnitude higher compared to that of the device fabricated under the worst deposition condition. The highest value of responsivity extracted was 0.24 A/W, which is comparable to the earlier reported values for $MAPbI_3$-based photodetectors and commercial Si photodetectors (< 0.2 A/W), and specific detectivity of 6.62×10^{11} Jones. (Figure 3.5c and d) Although the optimum deposition conditions acquired with our analysis may not be directly transferred to other deposition systems due to variations in experimental conditions, the methodologies demonstrated here, along with our analysis results, can be applied to any

deposition systems. Furthermore, our work demonstrates the advantage of DOE process for its accuracy in the predictability of the photodetector responsivity values under various deposition conditions and the efficiency of the device optimization process which requires only a small number of experiments.

3.3. Experiments

Synthesis of a MAPbI₃ Single Crystal Powder: The MAPbI$_3$ single crystal powders were synthesized as previously reported. 2.66 g of PbO (99.9% trace metal basis, Sigma-Aldrich) and 1.90 g of CH$_3$NH$_3$I (MAI, 99.5%, Greatcellsolar) were mixed and dissolved into a mixture of 18 ml hydriodic acid (HI, 57 wt% in water, TCI-Sejin CI) solution and 2 ml hypophosphorous acid (H3PO2, 50 wt% in water, Thermo Fisher) solution. The solution was heated at 130 °C on a hotplate until the precipitates completely disappeared. Then, the solution was cooled at room temperature to precipitate a MAPbI$_3$ single crystal powder. The single crystal powder was filtrated with filter paper and dried in a vacuum condition.

Perovskite Film Evaporation: The thermally grown 270 nm thick SiO$_2$ on Si and glass were used as substrates. The substrates were sequentially sonicated in acetone, 2-propanol, and deionized water for 10 min each. Then, the SiO$_2$ and glass substrates were cleaned using O$_2$ plasma treatment for 120 seconds. For flash evaporation, the synthesized MAPbI$_3$ powder was loaded onto a tungsten boat in a vacuum chamber. The cleaned substrates were placed into the chamber at a height of 30 cm from the source material. Then, the chamber was evacuated to a pressure of Torr. The tungsten boat was rapidly heated by applying a current of 100 A. The source powder was fully evaporated within 30 s.

Characterization and Measurement: Scanning electron microscopy (SEM): The images of the perovskite film were captured using JSM-7800F Prime at 5-10 kV.

X-ray diffraction (XRD): Crystallographic structures of perovskite films were analyzed by high-resolution X-ray diffractometer (HRXRD) technique (Rigaku Smartlab).

Rietveld refinement: XRD patterns were subject to Rietveld refinement using the GSAS-II [34] software for phase quantification. Strong preferred orientations of the deposited films required use of the March-Dollase function; peak broadening was treated with the domain size model due to the relatively small grain sizes (approx. 50 nm via SEM).

Photoluminescence (PL) spectroscopy: Steady-state PL spectra were measured using a spectrofluorometer (JASCO FP-8500) with a 520 nm excitation source.

UV-visible absorbance spectroscopy: Absorbance spectra were measured using a UV/Vis spectrophotometer (PerkinElmer LAMBDA 45).

Atomic force microscopy (AFM): The perovskite layer surface was characterized by an atomic force microscope system (NX 10 AFM, Park Systems).

Device fabrication: In order to fabricate photodetector, Au electrodes with a thickness of 50 nm were deposited on the prepared perovskite film by electron-beam evaporator through a shadow mask. The channel length and width of the fabricated photodetector were 50 μm and 1 mm.

Device measurement: The perovskite photodetector characteristics were measured using a semiconductor parameter analyzer (Keithley 4200 SCS). All the measurements were performed in a vacuum environment.

Data Analysis: All data were analyzed by a statistical analysis program (SAS JMP Pro 15).

3.4. Conclusion

I have employed DOE approach for systematically investigating the deposition conditions and film properties of single-source flash-evaporated $MAPbI_3$ films with the

aim of optimizing photodetector device performance. In total, OHP films were deposited under 15 different experimental conditions specified by three input variables -source mass, excess MAI, and heating current- selected by the Box-Behnken design to map various response variables that represent the structural and photophysical properties of the deposited films and photodetector device parameters. The correlations between the different film and device properties were investigated by using both a correlation matrix plot and regression analysis that enabled a detailed multivariate analysis. Our analysis reveals a significant interaction between the variables, which indicates a complex nature of the relationships between each film property and the input variables. Therefore, a simultaneous consideration of the variables via a multivariate approach is essential for optimizing the film deposition conditions, which cannot be achieved with a commonly practiced one-variable-at-a-time method. I have fabricated photodetector devices with the optimized deposition conditions predicted from the regression model (showing a responsivity value of 112.2 mA/W), which can be accurately predicted from the regression analysis. Overall, our work promotes DOE approach as an efficient statistical tool for optimizing perovskite film deposition conditions and a reliable route for extracting information on multi-dimensional relationships between material and device properties, which can be expanded to other complex optimization problems remaining in the general materials and device communities.

References

[1] Hwang B and Lee J-S 2019 *Adv. Opt. Mater.* **7** 1801356

[2] Tan Z-K, Moghaddam R S, Lai M L, Docampo P, Higler R, Deschler F, Price M, Sadhanala A, Pazos L M, Credgington D, Hanusch F, Bein T, Snaith H J and Friend R H 2014 *Nat. Nanotechnol.* **9** 687-92

[3] Choi H, Mai C-K, Kim H-B, Jeong J, Song S, Bazan G C, Kim J Y and Heeger A J 2015 *Nat. Commun.* **6** 7348

[4] Lee H-D, Kim H, Cho H, Cha W, Hong Y, Kim Y-H, Sadhanala A, Venugopalan V, Kim J S, Choi J W, Lee C-L, Kim D, Yang H, Friend R H and Lee T-W 2019 *Adv. Funct. Mater.* **29** 1901225

[5] Blancon J C, Tsai H, Nie W, Stoumpos C C, Pedesseau L, Katan C, Kepenekian M, Soe C M M, Appavoo K, Sfeir M Y, Tretiak S, Ajayan P M, Kanatzidis M G, Even J, Crochet J J and Mohite A D 2017 *Science* **355** 1288

[6] Park N-G 2018 *MRS Bull.* **43** 527-33

[7] Nie W, Tsai H, Asadpour R, Blancon J-C, Neukirch A J, Gupta G, Crochet J J, Chhowalla M, Tretiak S, Alam M A, Wang H-L and Mohite A D 2015 *Science* **347** 522

[8] Tsai H, Nie W, Blancon J-C, Stoumpos C C, Asadpour R, Harutyunyan B, Neukirch A J, Verduzco R, Crochet J J, Tretiak S, Pedesseau L, Even J, Alam M A, Gupta G, Lou J, Ajayan P M, Bedzyk M J, Kanatzidis M G and Mohite A D 2016 *Nature* **536** 312-6

[9] Yang W S, Noh J H, Jeon N J, Kim Y C, Ryu S, Seo J and Seok S I 2015 *Science* **348** 1234

[10] Fang Y, Dong Q, Shao Y, Yuan Y and Huang J 2015 *Nat. Photonics* **9** 679-86

[11] Zhou H, Chen Q, Li G, Luo S, Song T-b, Duan H-S, Hong Z, You J, Liu Y and Yang Y 2014 *Science* **345** 542

[12] Zhao X and Tan Z-K 2020 *Nat. Photonics* **14** 215-8

[13] Xing G, Mathews N, Lim S S, Yantara N, Liu X, Sabba D, Grätzel M, Mhaisalkar S and Sum T C 2014 *Nat. Mater.* **13** 476-80

[14] Cho H, Jeong S-H, Park M-H, Kim Y-H, Wolf C, Lee C-L, Heo J H, Sadhanala A, Myoung N, Yoo S, Im S H, Friend R H and Lee T-W 2015 *Science* **350** 1222

[15] Cao Y, Wang N, Tian H, Guo J, Wei Y, Chen H, Miao Y, Zou W, Pan K, He Y, Cao H, Ke Y, Xu M, Wang Y, Yang M, Du K, Fu Z, Kong D, Dai D, Jin Y, Li G, Li H, Peng Q, Wang J and Huang W 2018 *Nature* **562** 249-53

[16] Qian L, Sun Y, Wu M, Xie D, Ding L and Shi G 2017 *Adv. Mater.* **29** 1606175

[17] Dou L, Yang Y, You J, Hong Z, Chang W-H, Li G and Yang Y 2014 *Nat. Commun.* **5** 5404

[18] Kang K, Ahn H, Song Y, Lee W, Kim J, Kim Y, Yoo D and Lee T 2019 *Adv. Mater.* **31** 1804841

[19] Hwang B and Lee J-S 2017 *Sci. Rep.* **7** 673

[20] Wang J, Senanayak S P, Liu J, Hu Y, Shi Y, Li Z, Zhang C, Yang B, Jiang L, Di D, Ievlev A V, Ovchinnikova O S, Ding T, Deng H, Tang L, Guo Y, Wang J, Xiao K, Venkateshvaran D, Jiang L, Zhu D and Sirringhaus H 2019 *Adv. Mater.* **31** 1902618

[21] Senanayak S P, Yang B, Thomas T H, Giesbrecht N, Huang W, Gann E, Nair B, Goedel K, Guha S, Moya X, McNeill C R, Docampo P, Sadhanala A, Friend R H and Sirringhaus H 2017 *Sci. Adv.* **3** e1601935

[22] Yu W, Li F, Yu L, Niazi M R, Zou Y, Corzo D, Basu A, Ma C, Dey S, Tietze M L, Buttner U, Wang X, Wang Z, Hedhili M N, Guo C, Wu T and Amassian A 2018 *Nat. Commun.* **9** 5354

[23] Park N-G 2015 *Mater. Today* **18** 65-72

[24] Niu L, Liu X, Cong C, Wu C, Wu D, Chang T R, Wang H, Zeng Q, Zhou J, Wang X, Fu W, Yu P, Fu Q, Najmaei S, Zhang Z, Yakobson B I, Tay B K, Zhou W, Jeng H T, Lin H, Sum T C, Jin C, He H, Yu T and Liu Z 2015 *Adv. Mater.* **27** 7800-8

[25] Lan C, Dong R, Zhou Z, Shu L, Li D, Yip S and Ho J C 2017 *Adv. Mater.* **29** 1702759

[26] Momblona C, Gil-Escrig L, Bandiello E, Hutter E M, Sessolo M, Lederer K, Blochwitz-Nimoth J and Bolink H J 2016 *Energy Environ. Sci.* **9** 3456-63

[27] Mitzi D B, Prikas M T and Chondroudis K 1999 *Chem. Mater.* **11** 542-4

[28] Chen Y, Zhang L, Zhang Y, Gao H and Yan H 2018 *RSC Adv.* **8** 10489-508

[29] Li G, Ho J Y L, Wong M and Kwok H-S 2016 *physica status solidi (RRL) – Rapid Research Letters* **10** 153-7

[30] Ávila J, Momblona C, Boix P P, Sessolo M and Bolink H J 2017 *Joule* **1** 431-42

[31] Sessolo M, Momblona C, Gil-Escrig L and Bolink H J 2015 *MRS Bull.* **40** 660-6

[32] Crane M J, Kroupa D M, Roh J Y, Anderson R T, Smith M D and Gamelin D R 2019 *ACS Applied Energy Materials* **2** 4560-5

[33] Du P, Li J, Wang L, Liu J, Li S, Liu N, Li Y, Zhang M, Gao L, Ma Y and Tang J 2019 *ACS Appl. Mater. Interfaces* **11** 47083-90

[34] Liu M, Johnston M B and Snaith H J 2013 *Nature* **501** 395-8

[35] Ono L K, Wang S, Kato Y, Raga S R and Qi Y 2014 *Energy Environ. Sci.* **7** 3989-93

[36] Yang D, Yang Z, Qin W, Zhang Y, Liu S and Li C 2015 *J. Mater. Chem. A* **3** 9401-5

[37] Chen C-W, Kang H-W, Hsiao S-Y, Yang P-F, Chiang K-M and Lin H-W 2014 *Adv. Mater.* **26** 6647-52

[38] Hwang B and Lee J-S 2017 *Adv. Mater.* **29** 1701048

[39] Fan P, Gu D, Liang G-X, Luo J-T, Chen J-L, Zheng Z-H and Zhang D-P 2016 *Sci. Rep.* **6** 29910

[40] Longo G, Gil-Escrig L, Degen M J, Sessolo M and Bolink H J 2015 *Chem. Commun.* **51** 7376-8

[41] Xu H, Wu Y, Xu F, Zhu J, Ni C, Wang W, Hong F, Xu R, Xu F, Huang J and Wang L 2016 *RSC Adv.* **6** 48851-7

[42] Lohmann K B, Patel J B, Rothmann M U, Xia C Q, Oliver R D J, Herz L M, Snaith H J and Johnston M B 2020 *ACS Energy Lett.* **5** 710-7

[43] Kuehl R O and Kuehl R 2000

[44] Antony J 2014 *Design of experiments for engineers and scientists*: Elsevier)

[45] Tyagi P, David T W, Stoichkov V D and Kettle J 2019 *Sol. Energy* **193** 12-9

[46] Gunst R F 1996 *Technometrics* **38** 284-6

[47] *Response Surfaces, Mixtures, and Ridge Analyses,* pp 509-33

[48] Ferreira S L C, Bruns R E, Ferreira H S, Matos G D, David J M, Brandão G C, da Silva E G P, Portugal L A, dos Reis P S, Souza A S and dos Santos W N L 2007 *Anal. Chim. Acta* **597** 179-86

[49] Ando Y, Ohishi Y, Suzuki K, Suzuki A and Oku T 2018 *AIP Conference Proceedings* **1929** 020003

[50] McCusker L, Von Dreele R, Cox D, Louër D and Scardi P 1999 *J. Appl. Crystallogr.* **32** 36-50

[51] Von Dreele R 1997 *J. Appl. Crystallogr.* **30** 517-25

[52] Song Z, Watthage S C, Phillips A B, Tompkins B L, Ellingson R J and Heben M J 2015 *Chem. Mater.* **27** 4612-9

[53] Daniel M K, Matthew J C and Daniel R G 2019 Single-source flash sublimation of metal-halide semiconductors(vol 11084)

[54] Fang Y, Armin A, Meredith P and Huang J 2019 *Nat. Photonics* **13** 1-4

[55] García de Arquer F P, Armin A, Meredith P and Sargent E H 2017 *Nat. Rev. Mater.* **2** 16100

[56] Kanemitsu Y 2017 *J. Mater. Chem. C* **5** 3427-37

[57] Cao D H, Stoumpos C C, Malliakas C D, Katz M J, Farha O K, Hupp J T and Kanatzidis M G 2014 *APL Mater.* **2** 091101

[58] Hinds S, Levina L, Klem E J D, Konstantatos G, Sukhovatkin V and Sargent E H 2008 *Adv. Mater.* **20** 4398-402

[59] Taylor R 1990 *Journal of Diagnostic Medical Sonography* **6** 35-9

[60] Leng L, Zhang T, Kleinman L and Zhu W 2007 *J. Phys. Conf. Ser.* **78** 012084

[61] Shi Z, Zhang Y, Cui C, Li B, Zhou W, Ning Z and Mi Q 2017 *Adv. Mater.* **29** 1701656

[62] Jacobsson T J, Correa-Baena J-P, Halvani Anaraki E, Philippe B, Stranks S D, Bouduban M E F, Tress W, Schenk K, Teuscher J, Moser J-E, Rensmo H and Hagfeldt A 2016 *Journal of the American Chemical Society* **138** 10331-43

[63] Kim Y C, Jeon N J, Noh J H, Yang W S, Seo J, Yun J S, Ho-Baillie A, Huang S, Green M A, Seidel J, Ahn T K and Seok S I 2016 *Adv. Energy Mater.* **6** 1502104

[64] Wang L, McCleese C, Kovalsky A, Zhao Y and Burda C 2014 *Journal of the American Chemical Society* **136** 12205-8

[65] Geske T, Li J, Worden M, Shan X, Chen M, Bade S G R and Yu Z 2017 *Adv. Funct. Mater.* **27** 1702180

[66] Toby B H and Von Dreele R B 2013 *J. Appl. Crystallogr.* **46** 544-9

Chapter 4. Summary

In this thesis, I described that single source flash evaporation method is a facile method for depositing OHPs films. Our single source flash evaporation method also enables controlling film thickness and grain size by varying the amount of the source materials. In addition, it was possible to fabricate a film in a large area and found that it has statistical uniformity by utilizing the Tukey-Kramer test.

First, I demonstrated that photodetector devices fabricated by single source flash evaporation have comparable device performance to those fabricated by solution-based method. The fabricated devices showed the responsivity of 51 mA/W and detectivity of 9.55×10^{10} Jones which are comparable to the previously reported MAPbI$_3$-based photodetectors.

Secondly, I investigated that it was possible to control not only the physical properties such as grain size, purity and thickness of the film, but also electrical properties such as responsivity and detectivity by analyzing the correlation between the input variables and the response variables. The models created by the DOE approach could provide guidelines for optimizing the deposition conditions that produce high-quality perovskite films with the desired optoelectronic properties.

Finally, we studied the effect of the control variable was identified and optimized to improve the device performance about 2.5 times by creating a model using the design-of-experiment method. Moreover, the positive effect of PbI$_2$ on the photodetector was revealed by analyzing the intermediate process caused by the control of the input variable.

Our results demonstrate that single-source flash evaporation can be a promising route towards controllably and reliably depositing large-area perovskite films, and therefore producing perovskite-based optoelectronic devices in large-scale.

국문초록

플래시증착 페로브스카이트 기반 광검출기의 광전자 특성 예측 및 최적화 연구

이종훈
서울대학교 물리천문학부

오늘날, 유무기 페로브스카이트는 우수한 광학적, 전자적 장치에 대한 우수한 특성으로 인해 큰 주목을 받고 있습니다. 페로브스카이트 물질을 장치에 적용하기 위해서는 필름 형성과정이 필수적인 요소입니다. 용액 기반 필름 형성 방법, 화학기상증착법 및 열 증착법이 페로브스카이트 필름을 형성하기 위해 다양한 필름 형성방법으로 연구되고 있습니다. 용액 기반 필름 형성 방법 중 스핀코팅기술은 저렴하고 쉽게 접근이 가능한 공정이기 때문에 실험실 규모의 장치 제작에 주로 사용됩니다. 일부 연구에서는 스핀코팅으로 만들어낸 페로브스카이트 필름으로 높은 성능의 대면적 광전자 장치를 만들어내는데 성공했지만, 일반적으로 스핀코팅 기술은 넓은 영역에 재현성있고 균일한 필름을 형성하는데 큰 어려움을 겪고 있습니다.

이를 극복하기 위해 고안된 단일소스 플래시 증착기술은 증착하고자 하는 하나의 소스를 수 초 안에 빠르게 가열하여 페로브스카이트를 증착하는 대면적 박막증착 기술 중 하나입니다. 첫 연구에서는 단일소스 플래시 증착기술의 신뢰성과 두께 및 입자크기의 조절 가능성에 대해서 연구했습니다. 심화된 통계분석 방법을 이용하여, 플래시 증착기술을 통해 준비된 $MAPbI_3$ 필름이 4인치 웨이퍼 스케일 전체에 대해 균일한 두께와 매끄러운 표면을 가지고 있음을 검증했습니다. 이 증착방식을 활용했을 때, 소스의 양과 증착 단계의 수를 조절함으로서 필름의 두께와 입자 사이즈를 제어할 수 있다는

것을 보여주었습니다. 또 이 필름을 활용하여 광검출기 장치를 만들었을 때 대면적으로 동일한 성능을 가진다는 것 또한 통계적인 방법을 활용하여 확인했습니다.

일반적으로 증착 공정과 관련된 실험 변수의 복잡한 연관성으로 인해 고품질의 페로브스카이트 필름을 생산하기 위한 최적의 조건을 얻는 과정은 간단하지 않았습니다. 두 번째 연구에서는 실험의 횟수를 최소화하면서 최적화된 조건을 찾기 위한 효율적인 통계분석인 실험계획법을 활용하여 문제를 해결했습니다. 실험계획법으로 입력변수(소스 질량, MAI 첨가하는 몰 비율, 가열 전류)에 대한 광반응성, 필름 두께 및 순도에 대한 모델을 만들었으며, 이 모델을 통해 광검출기 장치를 최적화할 수 있었습니다. 더 나아가, 모델에서 사용한 입력변수만을 조절하여 장치를 만들었을 때, 최적화과정을 거치지 않은 장치보다 10배 더 향상된 112.2ma/W의 광반응성을 가지는 장치를 만들어냈습니다. 실험계획법을 사용하여 얻어낸 실험결과와 모델은 단순히 광반응성의 향상시키는 조건을 찾을 뿐만 아니라, 플래시 증착기술의 가변가능한 영역을 탐색함으로서다면적으로 필름의 품질을 향상시키기 위한 지침으로 활용될 가능성을 가지고있습니다.